University of Louisiana at Lafayette
Department of Civil Engineering

UNIVERSITY of LOUISIANA LAFAYETTE | Department of Civil Engineering

Final Report **June 2018**

Improvement of Concrete Bridge Girder Serviceability through Strengthening with Near-Surface Mounted (NSM) Shape Memory Alloys

PI:
Jovan Tatar, Ph.D.

Research Assistant:
Arkabrata Sinha

Department of Civil Engineering
University of Louisiana at Lafayette
131 Rex Street
Lafayette, Louisiana 70504

Sponsor:
Louisiana Transportation Research Center (LTRC)

Contract:
UL Lafayette Project No. 360136
LTRC Project No. 18-2TIRE

TECHNICAL REPORT STANDARD PAGE

. Report No.	2. Government Accession No.	3. Recipient's Catalog No.
4. Title and Subtitle **Improvement of Concrete Bridge Girder Serviceability through Strengthening with Near-Surface Mounted (NSM) Shape Memory Alloys**	5. Report Date 06/30/2018 6. Performing Organization Code LTRC Project Number: 18-2TIRE SIO Number: DOTLT1000191	
7. Author(s) Jovan Tatar, Ph.D. and Arkabrata Sinha	8. Performing Organization Report No.	
9. Performing Organization Name and Address Department of Civil and Engineering University of Louisiana at Lafayette Baton Rouge, LA 70803	10. Work Unit No. 11. Contract or Grant No.	
12. Sponsoring Agency Name and Address Louisiana Department of Transportation and Development P.O. Box 94245 Baton Rouge, LA 70804-9245	13. Type of Report and Period Covered **Final Report** **July 2017-June 2018** 14. Sponsoring Agency Code	

15. Supplementary Notes
Conducted in Cooperation with the U.S. Department of Transportation, Federal Highway Administration

16. Abstract

In 2017, American Society of Civil Engineers (ASCE) reported that 9.1% of national bridges are classified as structurally deficient. Many of these bridges are concrete bridges that also suffer from girder serviceability issues such as excessive deflections and cracking. In response to this problem, external post-tensioning techniques utilizing steel tendons and carbon-fiber-reinforced polymer (CFRP) were developed. External post-tensioning induces an uplifting force in the girder that results in a reduction of deflections and crack widths. The external post-tensioning techniques are, however, expensive in terms of material costs, energy expenditures, construction time, lane closure times, etc. Application of anchorage in-situ is an additional hurdle that further drives up the costs. In this study, a novel post-tensioning technique utilizing shape-memory alloys (SMAs) is proposed. SMAs are a class of alloys that have two material phases: the low-temperature phase – martensite; and the high-temperature phase – austenite. When martensite is plastically deformed, SMA can regain its original shape through heating, and the subsequent transformation from martensite to austenite occurs. The proposed post-tensioning method employs prestrained near-surface-mounted (NSM) NiTiNb wires that are heated to induce shape-recovery of the NiTiNb and generate post-tensioning in the strengthened concrete girders. To determine the feasibility of upscaling the proposed method a series of experiments were performed: (1) tensile tests on austenite to determine the stress-strain behavior of NiTiNb; (2) restrained recovery tests to characterize the post-tensioning potential of NiTiNb; (3) NiTiNb-grout bond characterization tests on notched plain concrete beam specimens; and (4) post-tensioning and flexural tests on reinforced concrete girders to verify the performance of the post-tensioning technique in structural-scale girders. Tensile tests on austenite indicated that the material has an initial elastic modulus of 10,000 ksi, with initial plastic deformation limit (detwinning) of approximately 85 ksi, and ultimate strength of approximately 150 ksi. Under the restrained recovery test, 2.5% prestrained NiTiNb wires achieved a maximum recovery stress of 73 ksi at 150 °C. Following cooling to ambient temperature, the wires retained about 92% of the maximum recovery stress, or 67 ksi. Bond characterization tests revealed poor bond between the grout and NiTiNb which negatively affected the transfer of post-tensioning force and strength of the plain concrete specimens; however, implementation of an anchorage device utilizing strand chucks significantly improved the behavior. Post-tensioning the cracked reinforced concrete girders reduced the crack width and residual midspan deflection by 74% and 0.06 in., respectively. Subsequent loading of the post-tensioned girders to failure indicated an increase in the yield moment and the ultimate moment capacity of the girders by up to 58% and 45% over control girder without NiTiNb, respectively. Overall, the proposed post-tensioning technique was successful in strengthening the structural-scale girders.

17. Key Words	18. Distribution Statement
Shape-memory alloys; NiTiNb; post-tensioning; concrete; repair; strengthening; bridge.	**Unrestricted. This document is available through the National Technical Information Service, Springfield, VA 21161.**

19. Security Classif. (of this report)	20. Security Classif. (of this page)	21. No. of Pages	22. Price
N/A	N/A	96	N/A

Improvement of Concrete Bridge Girder Serviceability through Strengthening with Near-Surface Mounted (NSM) Shape Memory Alloys

by

PI: Jovan Tatar, Ph.D.
Research Assistant: Arkabrata Sinha

Department of Civil Engineering
University of Louisiana at Lafayette
Lafayette, LA 70503

LTRC Project No. 18-2TIRE
SIO No. DOTLT1000191

conducted for

Louisiana Department of Transportation and Development
Louisiana Transportation Research Center

June 2018

ACKNOWLEDGMENTS

The authors thank the Louisiana Transportation Research Center (LTRC) for funding the research presented in this report. The authors also thank research assistants at UL Lafayette, Syed Ahnaf Morshed, Shagata Das, Tyler Young, and Peter Murphy for their help with specimen preparation and testing. Authors are especially grateful to lab manager, Mark LeBlanc, for his assistance with all aspects of the presented work.

TABLE OF CONTENTS

LIST OF FIGURES

LIST OF TABLES

ABSTRACT

In 2017, American Society of Civil Engineers (ASCE) reported that 9.1% of national bridges are classified as structurally deficient. Many of these bridges are concrete bridges that also suffer from girder serviceability issues such as excessive deflections and cracking. In response to this problem, external post-tensioning techniques utilizing steel tendons and carbon-fiber-reinforced polymer (CFRP) were developed. External post-tensioning induces an uplifting force in the girder that results in a reduction of deflections and crack widths. The external post-tensioning techniques are, however, expensive in terms of material costs, energy expenditures, construction time, lane closure times, etc. Application of anchorage in-situ is an additional hurdle that further drives up the costs. In this study, a novel post-tensioning technique utilizing *shape-memory alloys* (SMAs) is proposed. SMAs are a class of alloys that have two material phases: the low-temperature phase – martensite; and the high-temperature phase – austenite. When martensite is plastically deformed, SMA can regain its original shape through heating, and the subsequent transformation from martensite to austenite occurs. The proposed post-tensioning method employs prestrained near-surface-mounted (NSM) NiTiNb wires that are heated to induce shape-recovery of the NiTiNb and generate post-tensioning in the strengthened concrete girders. To determine the feasibility of upscaling the proposed method a series of experiments were performed: (1) tensile tests on austenite to determine the stress-strain behavior of NiTiNb; (2) restrained recovery tests to characterize the post-tensioning potential of NiTiNb; (3) NiTiNb-grout bond characterization tests on notched plain concrete beam specimens; and (4) post-tensioning and flexural tests on reinforced concrete girders to verify the performance of the post-tensioning technique in structural-scale girders. Tensile tests on austenite indicated that the material has an initial elastic modulus of 10,000 ksi, with initial plastic deformation limit (detwinning) of approximately 85 ksi, and ultimate strength of approximately 150 ksi. Under the restrained recovery test, 2.5% prestrained NiTiNb wires achieved a maximum recovery stress of 73 ksi at 150 °C. Following cooling to ambient temperature, the wires retained about 92% of the maximum recovery stress, or 67 ksi. Bond characterization tests revealed poor bond between the grout and NiTiNb which negatively affected the transfer of post-tensioning force and strength of the plain concrete specimens; however, implementation of an anchorage device utilizing strand chucks significantly improved the behavior. Post-tensioning the cracked reinforced concrete girders reduced the crack width and residual midspan deflection by 74% and 0.06 in., respectively. Subsequent loading of the post-tensioned girders to failure indicated an increase in the yield moment and the ultimate moment capacity of the girders by up to 58% and 45% over control girder without NiTiNb, respectively. Overall, the proposed post-tensioning technique was successful in strengthening the structural-scale girders.

INTRODUCTION

ASCE Report Card for 2017 suggests that approximately 9.1% of national bridges are classified as structurally deficient. Many of the deficient bridges fail to meet the serviceability limit state requirements imposed on maximum permissible deflections and crack widths. Repair methods based on post-tensioning were developed to address the serviceability problems by installing external tendons on a structure to provide the uplifting force (Figure 1). These tendons can be made of steel or carbon fiber reinforced polymer (CFRP) composites (e.g., Figure 1). Even though effective in improving the serviceability and strength of the flexural members, the technique is expensive in terms of material costs, energy expenditures, construction time, lane closure times, etc. Additionally, transfer of force between the external tendon and the flexural member is solely dependent on the proper anchorage of the prestressing cables which, if not executed properly, can lead to significant problems in the long term. Based on a similar concept, methods to post-tension concrete bridge girders implementing near surface mounted (NSM) prestressed CFRP strips and bars were developed (Figure 2). The main complication with their widespread adoption are ineffective, expensive, and difficult-to-construct anchorages. There is a need, thus, for a more economical and sustainable method to address the serviceability issues in concrete bridges.

This work seeks to verify the feasibility of using heat-induced post-tensioning in existing cracked reinforced concrete girders through the implementation of shape-memory alloys (SMAs) that can recover their original shape upon heating above the material's transformation temperature. In this study, near-surface mounted (NSM) NiTiNb alloy wires were evaluated for post-tensioning of bridge girders without the conventionally experienced problems with anchorages, high construction costs, long lane closure times, long construction times, etc. The experimental program consisted of a series of materials characterization tests on NiTiNb wires, bond characterization tests on plain concrete beams, post-tensioning tests on cracked reinforced concrete girders, and flexural tests on the post-tensioned girders.

Figure 1. External post-tensioning [Structural Group, Inc. 2016].

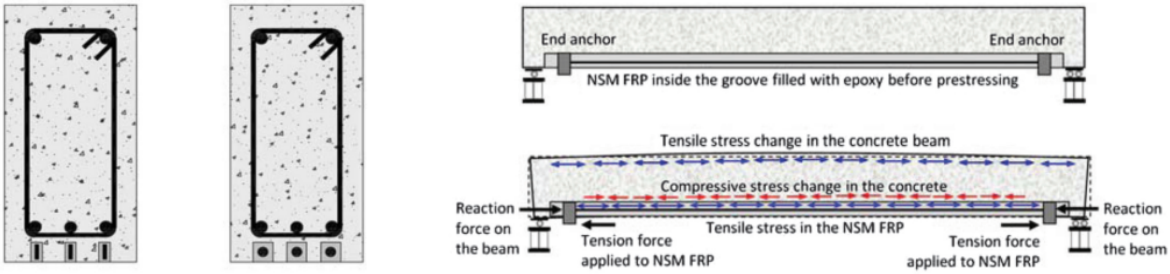

(a) (b)

Figure 2. (a) Near-surface mounted (NSM) FRP reinforcement; (b) Prestressed NSM FRP [1].

LITERATURE REVIEW

This section provides a short introduction to shape-memory alloys, and their unique shape-recovery properties – shape-memory effect and superelasticity. In addition, a state-of-the-art overview of SMA applications in civil engineering is provided. Finally, studies focusing on the bond characteristics between SMA and concrete are briefly summarized at the end of the chapter.

Shape Memory Alloys

Shape memory materials (SMM) are a class of materials which can recover their original shape from significant and seemingly permanent deformation when an external stimulus (e.g., heat) is applied. SMM may be alloys, also known as shape memory alloys (SMA), or polymers – shape memory polymers (SMP). SMAs are characterized with significantly higher strength and elastic modulus than SMP, which makes them uniquely suitable for a variety of structural applications.

SMAs have two material phases: (1) the high-temperature phase – austenite (cubic crystalline structure), and (2) low-temperature phase – martensite (tetragonal, orthorhombic, or monoclinic crystalline structure). The SMA can reversibly transform from one phase to the other when heated or cooled down through the transformation temperatures. The transformations occur over a temperature range (Figure 3a). During the cooling, the transformation from austenite to martensite starts at *martensitic start temperature* (M_s) and is completed at *martensitic finish temperature* (M_f) (Figure 3a-top). Similarly, the heating transformation from martensite to austenite begins at *austenitic start temperature* (A_s) and is finished at *austenitic finish temperature* (A_f) (Figure 3a-bottom). Transformation temperatures can be changed by tailoring the molar ratio of alloy elements in an SMA. Characterization of transformation temperatures is usually performed via differential scanning calorimetry (DSC). An example DSC curve for a SMA is shown in Figure 4.

Shape-memory Effect

Martensite can take two variants: (1) twinned martensite (in which crystals are oriented in varying directions); and (2) detwinned martensite (in which one crystal orientation is dominant). Transformation from twinned to detwinned martensite is accomplished by application of external stress; the detwinning is initiated at the *detwinning start stress* (σ_s), and the process is completed at *detwinning finish stress* (σ_f) (Figure 3b). Upon the release of external loading (from some stress greater than σ_f to 'zero' stress) the deformation of martensite's crystalline structure is retained (Figure 3c). Heating of the SMA to a temperature above A_f will then result in shape recovery through transformation of detwinned

martensite to austenite (Figure 3c) – such transformation is termed *reverse transformation*. Cooling of SMA to a temperature below M_f triggers transformation from austenite to twinned martensite – also known as *forward transformation*. The described behavior, named *shape-memory effect* (SME), is a one-way process: subsequent heating above A_f does not additionally alter the shape of SMA.

Shape memory effect exhibited by an SMA is shown as a function of stress, strain, and temperature in Figure 3d. Cooling of austenite to a temperature below M_f results in transformation from austenite to twinned martensite (Figure 3d from A to B). By applying external stress that exceeds σ_f, transformation to detwinned martensite is accomplished (Figure 3d from B to C). By releasing the applied stress, the SMA is then elastically unloaded to some permanent strain (Figure 3d from C to D). With subsequent heating of the SMA, the reverse transformation from detwinned martensite to austenite is initiated once A_s is reached (Figure 3d from D to E). When the SMA is at a temperature higher than A_f the full shape recovery is attained (Figure 3d point F). Once the heat source is removed, the forward transformation from austenite to martensite is accomplished once the temperature is below M_f.

The magnitude of transformation temperatures (M_s, M_f, A_s, A_f) increases with the applied load. The relationship between applied stress and transformation temperatures is schematically shown via a stress-temperature phase diagram in Figure 5. The increase in the magnitude of transformation temperatures under stress must be considered when SMAs are used as actuators: when reverse shape recovery is initiated in a constrained detwinned SMA, the A_s and A_f transformation temperatures will increase as the restrained *recovery stress* develops in the SMA with heating. This necessitates heating the SMA above the transformation temperature obtained via DSC (in an unstressed state) to achieve a complete reverse transformation and maximum recovery stress.

Another important property of SMAs in actuator applications is their *thermal hysteresis*, which is defined as a temperature difference between the A_s and M_s. In situations where it is desirable to retain the SMA recovery stress following removal of the heat source, it is required that the *service temperature* (T_s) which the SMA reaches upon cooling be much greater than M_s, or $T_s \gg M_s$. If this condition is not satisfied and M_f and/or M_s is/are lower than T_s, the SMA recovery stress could be completely lost during the cooling process due to the forward transformation (austenite to twinned martensite).

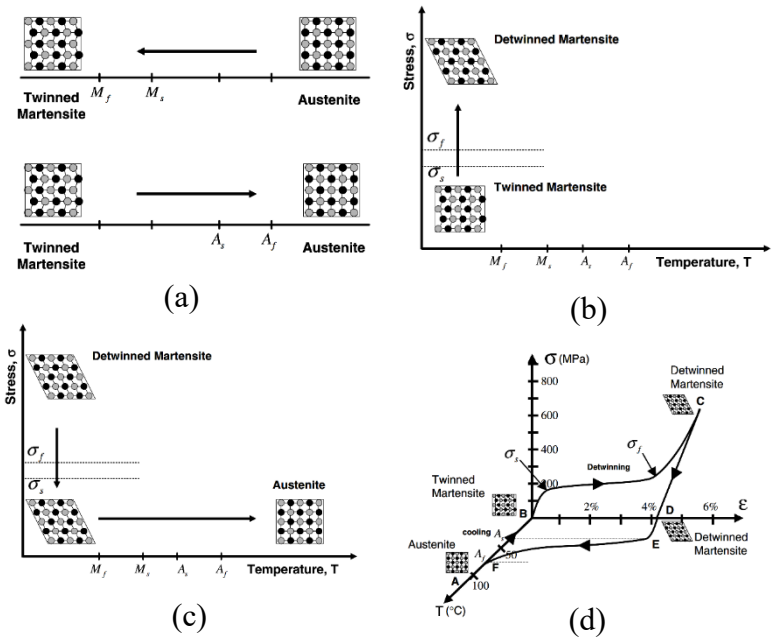

Figure 3. Thermomechanical characteristics of SMA: (a) Nitinol phase transformations; (b) transformation from twinned to detwinned martensite with external stress; (c) shape recovery of detwinned martensite through austenitic transformation; and (d) stress-strain-temperature diagram of nitinol [2].

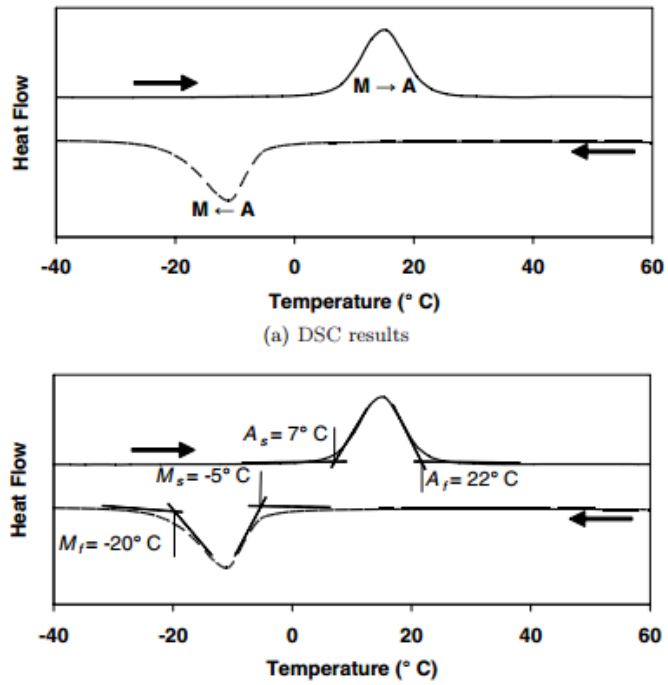

Figure 4. Example DSC curve of an SMA [2].

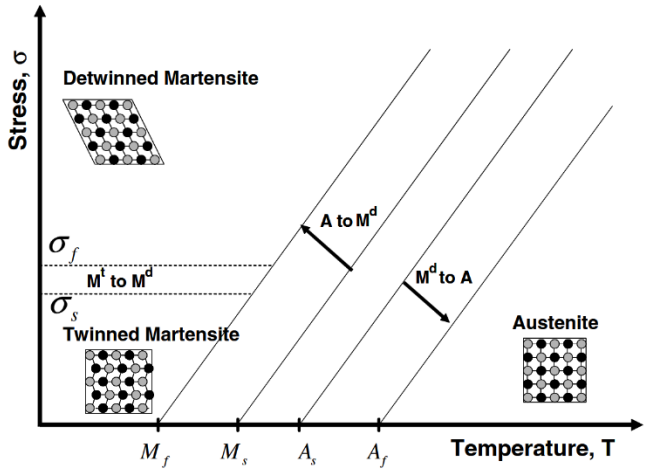

Figure 5. Stress-temperature phase diagram of SMA [2].

Superelasticity

In addition to SME, SMAs also possess another property that allows for shape recovery – superelasticity. When the material is in the austenite phase and a sufficiently large stress is applied to it, the SMA undergoes transformation to detwinned martensite. Upon release of the applied stress, the SMA returns to its original shape. The superelastic behavior is demonstrated in Figure 6. As stress is applied to the SMA, the transformation to detwinned martensite starts at stress σ^{M_s} and is complete at stress σ^{M_f}. As the external stress is released, the transformation back to austenite is initiated and completed when stress reaches σ^{A_s} and σ^{A_f}, respectively.

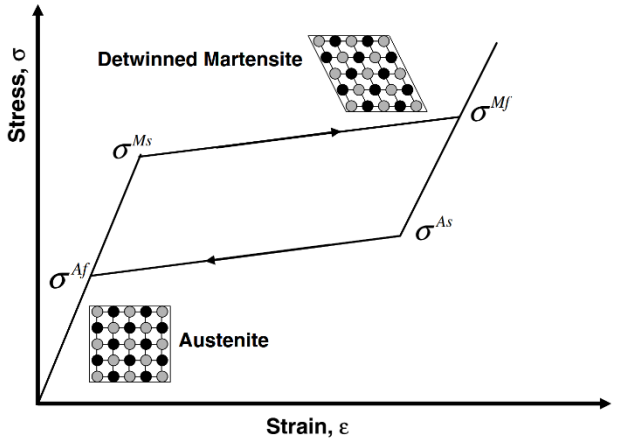

Figure 6. Superelastic stress-strain behavior of SMA [2].

Types of Shape Memory Alloys

The SMA generally contain two or three elements in their composition. The addition of a third element to *binary* SMA (SMA having two elements) results in a *ternary* SMA and can alter the properties of the base alloy. This gives the designers flexibility to choose from a large variety of SMAs, which can be applied to different problems in the industry. The third element is added to the binary SMA to modify their thermal properties like transformation temperature or the width of the thermal hysteresis. SMAs can also be classified into different categories based on the primary alloying element, mode of actuation (thermal, magnetic, etc.), operating temperatures and the desired behavior (SME or superelasticity). In the subsequent sections, the effect of the alloying element on the transformation temperature is primarily discussed, with particular emphasis on the *nickel-titanium-niobium* (*NiTiNb)* alloy, since that is the SMA which was used in this study [2].

Nickel-Titanium (NiTi)-Based Alloys

The binary NiTi SMA has been widely used in different commercial applications due to its excellent SME, superelasticity, resistance to corrosion and biocompatibility. Buehler et al. (1963) studied the SME in *equiatomic* (50 at. % of Ni and Ti) NiTi SMA and discovered that this alloy had the highest A_f out of all the NiTi based SMA. Increasing the amount of nickel by 1% over 50 at. % decreases the A_f by up to 40 ºC. However, decreasing the atomic percentage of nickel does not cause any change in the transformation temperatures [2].

For an SMA to be applied in structural engineering, it needs to have the minimum response to large differences in temperature, so that it can be safely transported and installed without being accidentally actuated by the ambient temperature. In structural engineering, the SME must be triggered when prestressing forces are required to repair damaged structures. When the SMA is used for their superelastic properties, the temperature of the SMA must be above the A_f temperature. Applying a stress above σ^{M_f} will convert the SMA to detwinned martensite phase and removing the subsequent removal of the load will cause superelastic recovery due to transformation to austenite phase. Hence, when an SMA is chosen for structural applications because of their SME, the thermal hysteresis needs to be sufficiently wide to avoid accidental triggering of SME as well as loss of prestressing force [2, 3].

The widening of the hysteresis loop can be achieved by adding a third element – *Niobium (Nb)* – to the existing binary NiTi alloy to form NiTiNb alloy. The widening of the thermal hysteresis occurs due to the partitioning of the strain into a recoverable part and an irrecoverable part. The recoverable strain is caused by the NiTi part and the irrecoverable strain is caused by the soft Nb part. Despite the widening of thermal hysteresis, the NiTiNb alloy has some residual strain when the pre-deformed alloy is actuated to trigger the SME.

An important factor which affects the width of the hysteresis is the amount of Nb in the ternary NiTiNb alloy. The NiTiNb alloys generally have a wider thermal hysteresis than NiTi alloys (M_s of -74.29 ºC and A_s of 122.5 ºC). A lower Nb content increases the width of the hysteresis loop by increasing the difference between the A_s and M_s. For example, $Ti_{46.9}Ni_{50.1}Nb_3$ (M_s of -68.15 ºC and A_s of -43.15 ºC) has a wider thermal hysteresis than $Ti_{44}Ni_{47}Nb_9$ (M_s of -73.15 ºC and A_s of -23.15 ºC) [2, 3].

There are other applications of SMAs, where they are used as micro-actuators e.g., sensors in structural health monitoring systems. In these circumstances, it is desirable to have a narrow mechanical hysteresis. A narrow mechanical hysteresis would make the material more sensitive to the changes in strain of the structure. The application of stress would lead to the development of strain in the SMA and causes a phase transformation which in turn would change the electrical resistance of the material.

Adding *copper (Cu)* to the binary NiTi alloy replaces the Ni to form NiTiCu alloys. Although the addition of Cu makes the hysteresis loop narrower, this also reduces the superelastic effect of the alloy by more than 50% when compared to the binary NiTi alloy. The Cu amount between 5 and 10 at. % is preferred for the choice of materials being used as actuators. When the Cu content is between 5 and 10 at. %, the material shows a clear phase transformation. A Cu amount greater than 10 at. % should be avoided as it tends to make the alloy lose its ductility[2, 4].

Some application of the SMA may require high A_f and stable operating conditions like for example, the core region of an aircraft engine or downhole applications in the oil and gas industry. This led to the development of a new type of SMA known as the *High-Temperature Shape Memory Alloy (HTSMA)* which were formed by the addition of ternary elements like *Palladium (Pd), platinum (Pt), Hafnium (Hf), Gold (Au) and Zirconium (Zr)* to the binary NiTi alloy. The addition of these materials results in A_f between 100 ºC to 800 ºC. The commercial application of alloys with ternary elements Pd and Pt have been limited due to the high material cost. Although alloys with ternary element Hf and Zr have a lower cost than the ones with Pt and Pd, they have lower A_f. A significant limitation of HTSMAs is their lower transformation strain (~3%) when compared to binary NiTi alloys [2, 5].

Copper (Cu)-Based Alloys

The Cu-based SMA became an attractive substitute for the NiTi SMA because of the lower cost as well as good electrical and thermal conductivity. These alloys usually have a narrower hysteresis than the NiTi alloys. The A_f of these alloys are highly dependent on their composition and a change in the atomic percentage of the order of 10 is required to change the A_f by 5 ºC.

The Cu-Zn based alloys are characterized by good ductility and resistance to intergranular fracture when compared to other Cu-based alloys. CuZnAl, which is obtained by adding a third element Aluminum (Al) was found to have a significantly higher M_s as compared to the binary alloys (e.g., increasing the Al content from 5 percentage by weight (5 wt. %) to 10 wt. % increases the M_s from -180 ºC to 100 ºC). CuZnAl has a transformation strain of about 3-4% and an operational temperature below 100 ºC. CuZnAl alloy shows complete shape recovery and superelasticity within stress levels of approximately 200 MPa.

Another type of Cu-based alloys is the CuAlNi which is formed by adding Nickel (Ni) to the binary CuAl alloy. Compared to the CuZn alloys, CuAlNi has lower ductility and is prone to intergranular cracking which leads the alloy to fracture at a stress of about 280 MPa. The transformation strain in this class of SMA is limited to 3%, and the alloy exhibits poor response to fatigue. The benefit of adding Ni to CuAl is that it makes the alloy less sensitive to stabilization (tendency to stay in martensite phase by increasing the reverse transformation temperature) and aging (treatment of alloys at high temperature which makes the properties change and settle very slowly). The transformation temperatures change with the amount of Ni and Al but, the relative change in the transformation temperatures is insignificant which makes the width of thermal hysteresis stay quite constant [2, 5].

Iron (Fe)-Based Alloys

Iron-based SMAs have found significant use in structural engineering applications due to their lower cost, wider thermal hysteresis, higher elastic stiffness, and ductility when compared to most NiTi-based SMAs; however, they have lower shape recovery strain (about 4%) as compared to NiTi and Cu-based alloys. Moreover, Fe-based alloys offer better workability, weldability, and machinability which make them attractive for larger and more complex engineering structures. The most common Fe-based SMAs are FeNiCoTi and FeMnSi [2, 6].

Cobalt (Co)-Based Alloys

CoNiAl alloy can be formed by adding cobalt (Co) to NiAl or Ni to CoAl binary alloy. Their application in structural engineering is limited because they possess a very low A_f (about -26 ºC) and a narrow thermal hysteresis. This alloy exhibits a transformation strain of about 4% when it is subject to thermal cycles and has stable superelastic behavior at a temperature sufficiently above the A_f. CoNiAl alloy has a unique property by which it can undergo a forward transformation due to magnetic-field-induced reorientation when subjected to magnetic fields. This makes it an attractive choice for applications where magnetic actuation is required [2, 7].

Applications of SMAs in Civil Engineering

Numerous applications of SMAs in civil engineering are reported in the literature. A brief overview of those studies is provided in this section.

Applications Utilizing Shape-Memory Effect

SMAs have been developed and used since the 1960s in a wide range of applications in medical, robotics, aerospace and in the automobile industries. One of the most notable applications of SMA is as actuators. For example, SMA actuators have found applications in robotic systems which require powerful, compact and lightweight actuators. As opposed to electric, hydraulic or other actuators which lose power when they are downscaled, the SMA actuators have a high strength to weight ratio, which makes them ideal for miniaturized applications. In one of these applications, straight SMA fibers were attached between two disks in an actuator with the intention of achieving amplified mechanical displacement. The disks were kept separated by preloaded springs, but when the SMA fibers were heated, they contracted by the SME and thus achieved mechanical displacement (Figure 7a, Figure 7b). The prospect of using SMA in structural engineering as a prestressing material by utilizing their SME and superelasticity properties have been recognized. Research is being conducted to determine the feasibility and effectiveness in such applications [8].

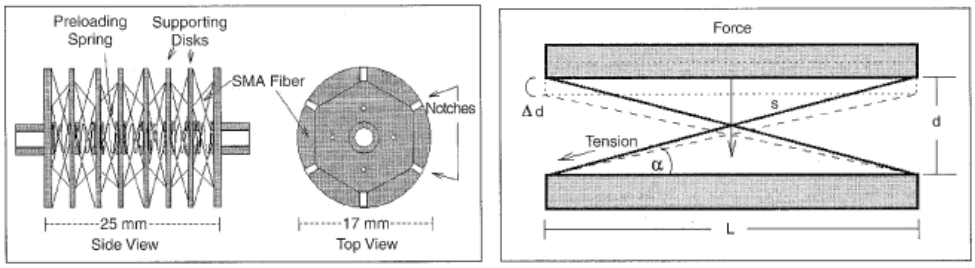

(a) (b)

Figure 7. SMA actuator showing: (a) the overall arrangement of the actuator; and (b) SME displayed in two disks connected by SMA fibers [8].

The advent of SMA in the buildings and infrastructure started with Soroushian et al. (2001) [9] who used Fe-based SMA rods to apply post-tensioning forces to repair damaged bridge girders. A methodology to repair the cracks caused by insufficient shear strength of a bridge girder was developed and verified in the laboratory. Implementation of this design was carried out in the field on an out-of-service bridge in Michigan (Figure 9). SMA rods were recovered in a restrained condition and the stress generated due to the restrained shape recovery was utilized to reduce the width of the shear cracks. Five SMA rods of 7⁄8 in. (22.2 mm) diameter were mounted externally across the cracks at an angle of 35 degrees on both

sides of the beam web (Figure 8). The SMA rods were heated in a retrained condition above their A_f by passing current, which resulted in a shape recovery and generation of recovery stress in the rods. Localized prestressing of the beam web via SMA rods resulted in a 40% reduction in crack width (from 0.022 in. to 0.013 in.). The rods developed a recovery stress of 120 MPa (17 ksi), which was 32% lower than the maximum measured recovery stress (176 MPa or 25 ksi) in the laboratory experiments. The loss in recovery stress was explained by relatively large slippage at the anchorage.

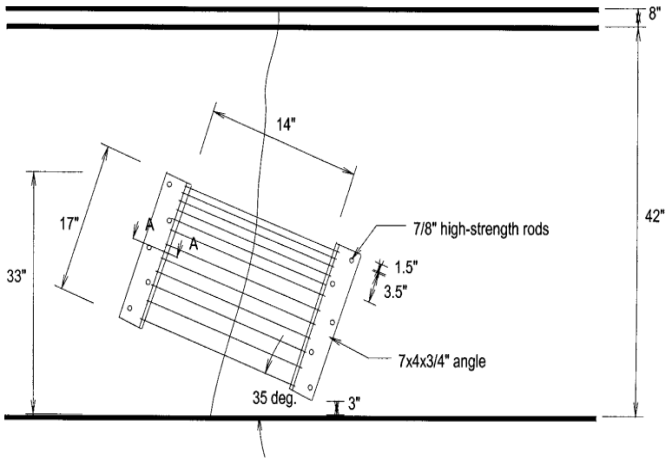

Figure 8. Schematic diagram for SMA rods used to control of shear cracks in a bridge girder [9].

Figure 9. SMA rods installed in a bridge girder in Michigan to control of shear cracks [9].

An experimental study on 1.5 ft. long concrete beams was conducted by Deng et al. (2006) [11] to evaluate the post-tensioning potential of 6-8% prestrained NiTi (50 wt. % Ti) wires by using their SME. The NiTi wires were embedded in the reinforced concrete beams by

inserting the wires in the forms before pouring concrete. A computer-based data acquisition and control system was used to record midspan deflection of the beam and the temperature in NiTi wires (Figure 10). The SME was initiated by heating the SMA wires via Ohmic heating. The recovery stress steadily increased until the wires reached the A_f temperature (40 ºC). The total upward beam displacement, due to the maximum recovery stress generated by the NiTi wires, was 0.41 mm. When the wires cooled down below A_f to room temperature, the transition from austenite to martensite occurred, and therefore the recovery stress dropped which caused the upward deflection of the beam to reduce from 0.41 mm to 0.36 mm (Figure 11a). The upward deflection depended on the actuation factors like the profile of current and actuation time. It was observed that a gradual increase of the current intensity from 37 A to 43 A in 150 minutes caused a greater reduction in the midspan deflection as compared to the condition where the current was increased stepwise from 0 A to 43 A over the same duration. The initial pre-strain also affects the recovery force; it was found that higher prestrain does not necessarily yield the highest recovery force (Figure 11b). A greater area of NiTi wires led to an increase in the recovery stress which increased the upward deflection.

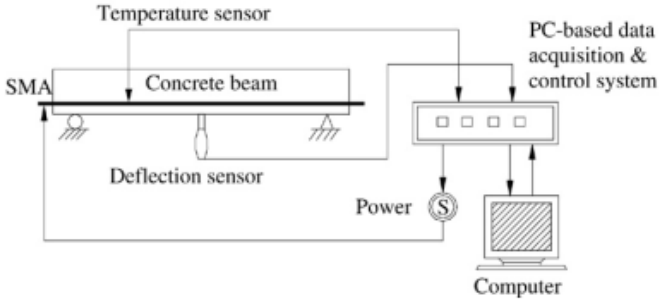

Figure 10. Experimental setup for study on NSM SMA [11].

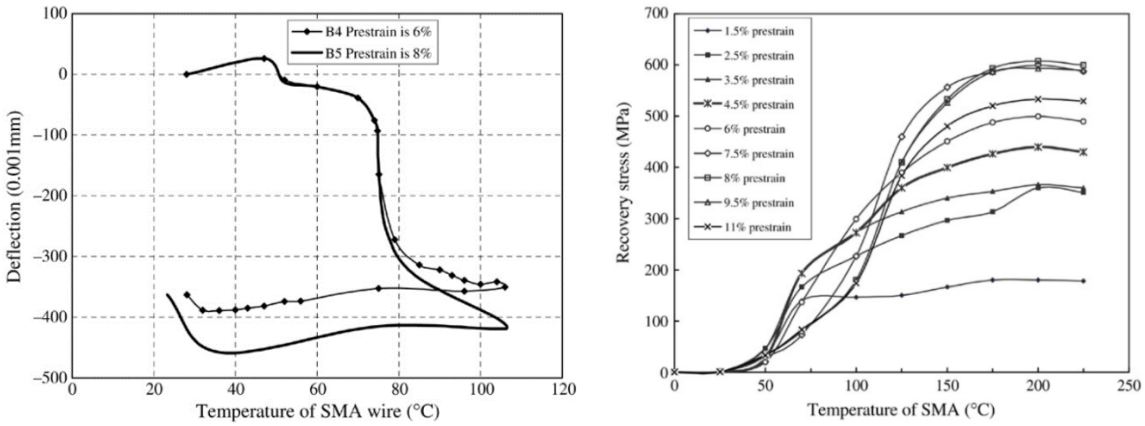

(a) (b)

Figure 11. Response to restrained heating of the NiTi wires: (a) Deflection vs. Temperature curve for different pre-strain; and (b) Recovery stress vs. Temperature curve of the wires [11].

Li et al. (2006) [12] experimentally evaluated the ability of SMA wires to control deflections in concrete beams. In this study, the SME of 2 mm diameter NiTi (50.8 wt. % Ni) wires was activated via Ohmic heating. In addition to this, the scope of this study also included carrying out permanent repair of the structures using carbon fiber reinforced polymer (CFRP) after initial repair with NiTi wires. The change in resistance of the NiTi wires was used to assess the midspan deflection of the beams. At first, 1.65 ft. long beams were loaded in a three-point bending setup to induce midspan cracking (Figure 12a). After inducing the cracks, the NiTi wires were actuated by passing constant currents of 14 A and 16 A. Actuation using a 16 A current generated more recovery stress than a 14 A current for the same temperature change. The test results showed a reduction of crack width from 3.98 mm to 0.65 mm following the shape recovery of NiTi wires. The specimens which had greater NiTi reinforcement ratio were more effective at reducing the midspan deflection and closing cracks. The specimen with 0.08% NiTi reinforcement ratio reduced the midspan deflection by about 58% whereas the specimen with 0.16% NiTi reinforcement ratio reduced the midspan deflection by about 73%.

From this study, the possibility of using SMA as a strain sensor emerged based on the observation that change in resistance of the SMA had a linear relationship with the midspan deflection of the beams. Strengthening of the repaired beams using CFRP plates increased the load carrying capacity of the specimens by up to 50% and hence, was considered a good permanent repair method.

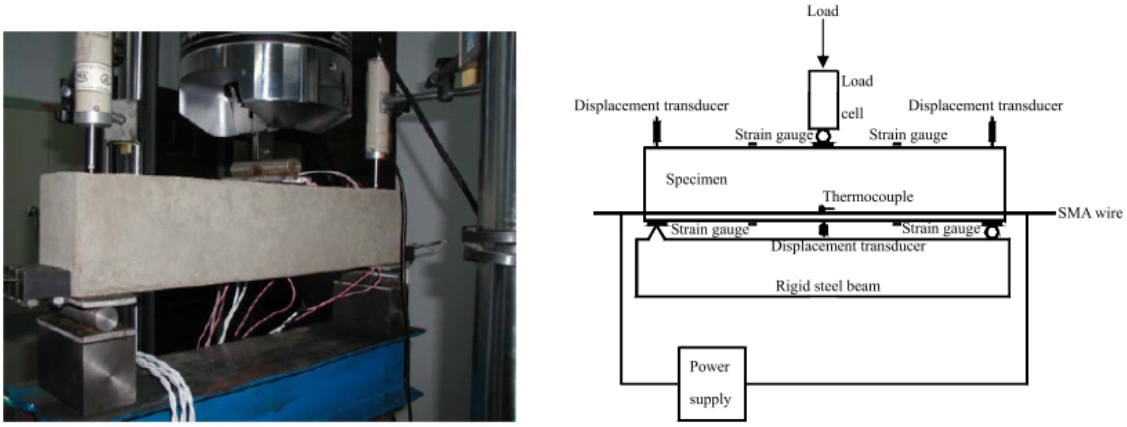

(a) (b)

Figure 12. Post-tensioning process showing: (a) test setup for three-point bending; and (b) schematic diagram of instrumentation for the test [12].

NiTiNb has a significantly wider thermal hysteresis than NiTi; thus, within the service temperatures typically experienced by civil infrastructure, the loss in the recovery stress at lower temperatures is minimal. Dommer and Andrawes (2012) [13] conducted thermomechanical characterization of NiTiNb wires to investigate the feasibility of using NiTiNb wires for active confinement of reinforced concrete columns by wrapping the wires spirally around the columns and applying transverse pressure (Figure 13). The results of short-term and long-term recovery tests (Figure 14a, Figure 14b) indicated that the NiTiNb wires could retain above 500 MPa of recovery stress over a wide range of temperatures (between -10 °C and 55 °C). The study explored resistive heating and torch heating as methods for triggering the SME. Both methods resulted in the generation of same recovery stress indicating that SME response is independent of the heating method. Based on these findings, the authors concluded that NiTiNb wires were suitable for active confinement of columns.

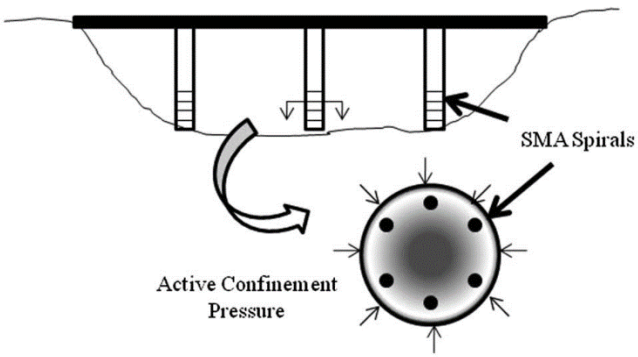

Figure 13. Schematic diagram of active confinement using SMA spirals [13].

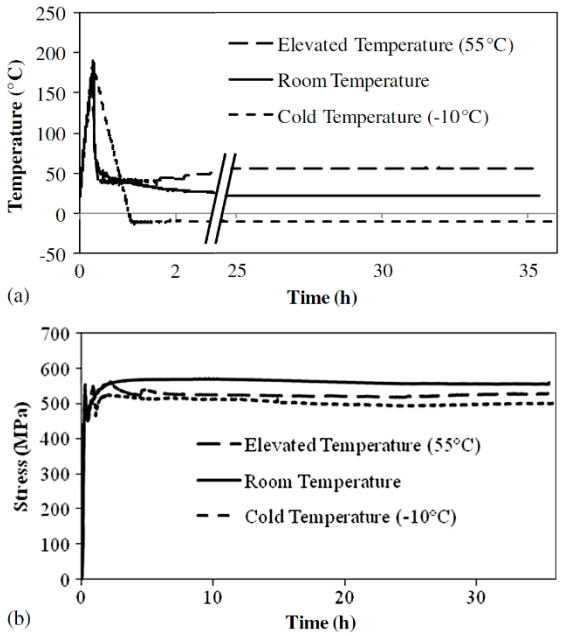

Figure 14. Thermomechanical behavior of NiTiNb wires showing: (a) Temperature vs. Time curve; and (b) Recovery Stress vs. Time curve under different temperature for the long-term test [13].

In another study, Andrawes et al. (2010) [14] compared cylinders with active confinement provided by the SME of the NiTiNb wires, and passive confinement provided by GFRP wraps. Some of the specimens had a combination of NiTiNb wire and GFRP confinement. First, thermomechanical characterization of 6.4% prestrained NiTiNb wires of 2 mm diameter was performed by conducting a restrained recovery test. The maximum recovery stress was found to be 565 MPa at a temperature of 108 °C, but the stress reduced to 470 MPa (by about 20%) after cooling down to a temperature of 16 °C. Evaluation of NiTiNb wires with different prestrains indicated that the recovery stress linearly increased with the prestrain (Figure 15). The recovery stress increased by 22% for with raise in prestrain from 2.8 to 6.4%

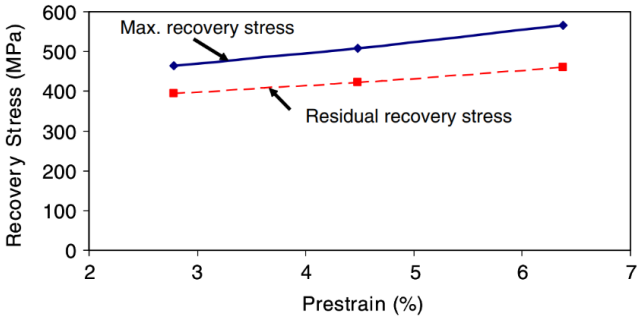

Figure 15. Recovery Stress vs. Prestrain curve for NiTiNb wires [14].

Concrete cylinders were tested in compression under a displacement-controlled loading rate of 1 mm/min. The cylinders remained intact even after experiencing significant cracking and crushing (Figure 16b) because of the active pressure applied by the NiTiNb spirals. During the compression test, as the specimen was experiencing excessive deformations, the NiTiNb spiral fractured suddenly and the cylinder failed diagonally (Figure 16c). Comparing the strengthening effect of active and passive NiTiNb-GFRP wrapped specimens, it was found that active confinement imparted greater strength than the passive confinement. The comparison between the hybrid (NiTiNb-GFRP) and GFRP confined specimens show that the peak strength offered by the two were almost identical, but the ultimate strain was increased in the hybrid sample due to the ductility offered by the NiTiNb wires. This study also provided a comparative analysis of the tensile strength of spliced NiTiNb wires connected using U-clamps, sleeves and welded connections (Figure 17). The U-clamps and the welded connections had the maximum and minimum tensile strength respectively.

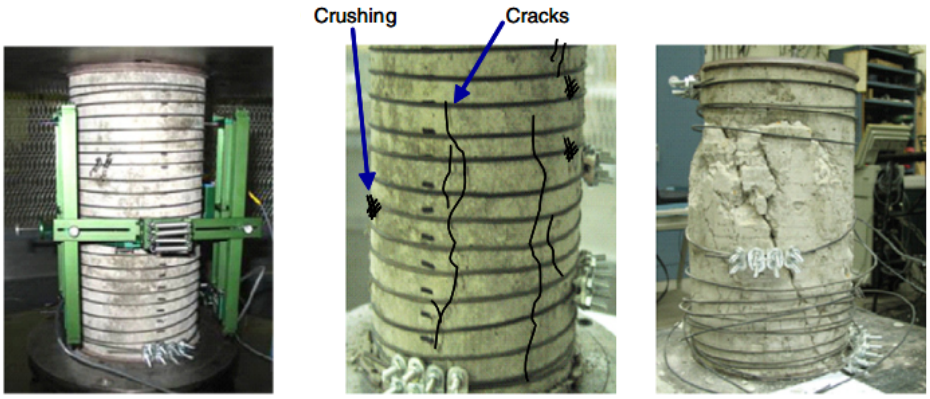

(a) (b) (c)

Figure 16. Active confinement of Shape Memory alloy during different stages of compression testing: (a) before applying compression; (b) during compression; and (c) after failure [14].

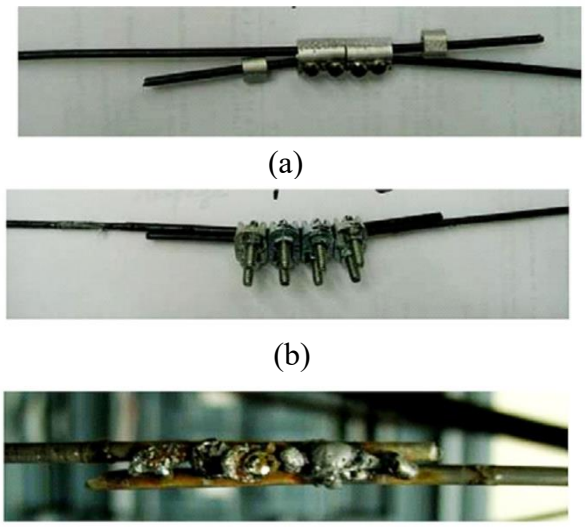

(a)

(b)

(c)

Figure 17. Different type of splices and connections: (a) sleeve connection; (b) U-clamp connection; and (c) welded connection [14].

Kotamala (2004) [16] studied the feasibility of using NiTi wires to prestress concrete beams with the aim of increasing their flexural capacity. The tensile tests indicated that ultimate strength and strain at failure were affected by the detwinning load and not by the temperature of the wires. The modulus of elasticity increased significantly for the wires in austenite phase (Figure 18).

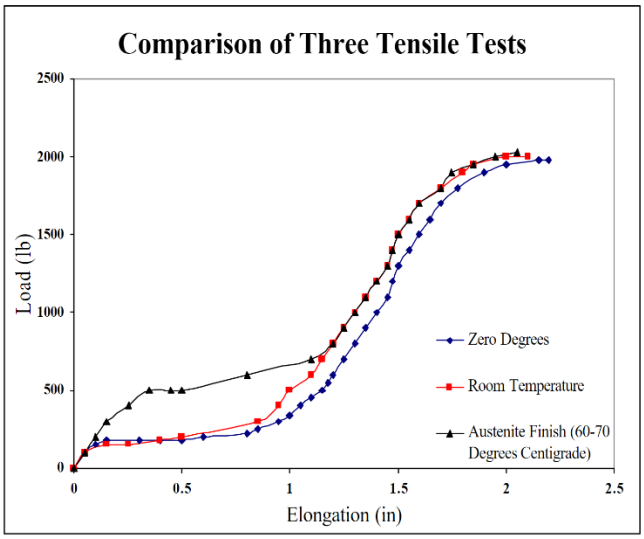

Figure 18. Tensile properties of NiTi wires at different temperatures [16].

In this study, prestressing was conducted on 20 in. long concrete beams which had a cross section of 3 in. x 6 in. NiTi wires of diameter 0.119 in. with 4% prestrain were eccentrically

placed in the concrete beams. Heating the NiTi wires above their A_f (60-70 ºC), by passing a 20 A current, generated 1335 lbf recovery force. Only 61% (810 lbf) of the recovery force was transferred to the concrete as the prestressing force. The loss in prestressing force was accredited to poor bond characteristics between the concrete and the SMA wires. However, it was observed that the overall flexural strength of the beams, prestressed with NiTi wires increased by almost 95 psi (Figure 19).

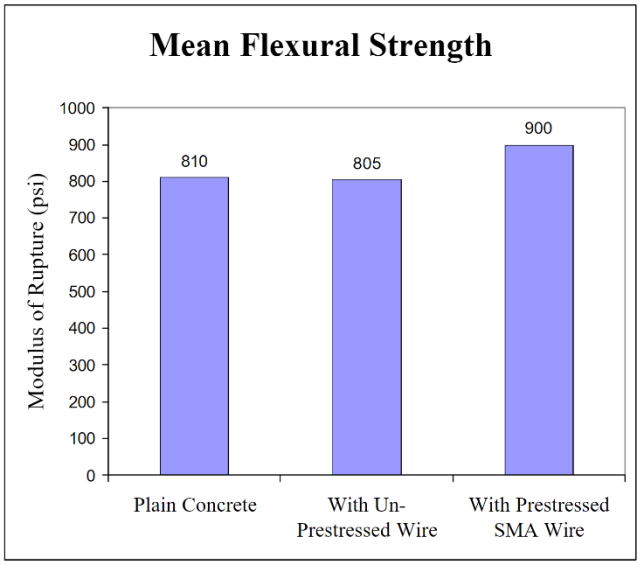

Figure 19. Comparison of flexural strength of beams [16].

The feasibility of self-post-tensioning bridge girders using the recovery stress generated from the restrained shape recovery of NiTiNb wires, when actuated via the heat of hydration of grouts, was investigated by Ozbulut et al. (2016) [17] (Figure 20). While using in-situ repair techniques, activating the NiTiNb wires using the heat of hydration of the grouts, which are used to fill the grooves in which the wires are installed, is easier than jacking or resistive heating. The NiTiNb wires utilized in the experiments had a relatively low reverse transformation temperature of 11 °C, which was activated by the heat of hydration of cementitious grouts (temperature goes up to 53 °C). The restrained recovery tests on 10% prestrained NiTiNb wires generated a sufficiently high recovery stress (above 500 MPa) which could be transferred to concrete as post-tensioning force. The amount of post-tensioning force generated can be adjusted in this self-post tensioned method by choosing grouts which generate different amounts of heat to bring about partial shape recovery.

The generation of the recovery stress depends on the temperature increment caused by the heat of hydration of the grout. The temperature should rise above the $A_f$to trigger complete shape recovery. Experiments on different grouts (Table 1) demonstrated that the maximum

rise in temperature was brought about by the Sika grout (53 °C). The rise in temperature by 53 °C was only sufficient transform SMA partially to the austenite phase causing incomplete shape recovery. The bond characteristics of the NiTiNb wires with the grout was obtained by conducting pullout tests on 3.5 mm diameter wires embedded in 102 mm x 102 mm cylindrical concrete specimens. The average bond stress was found to be 1.3 MPa and there was no significant slippage as observed from the digital image correlation results. It was concluded that NiTiNb SMA wires can be used in the self-post tensioning of concrete bridge girders with grouts that can raise the temperature of the wire above A_f. In addition to this, the grout provides higher resistance to corrosion of the NiTiNb wires and increases the service life of the structure.

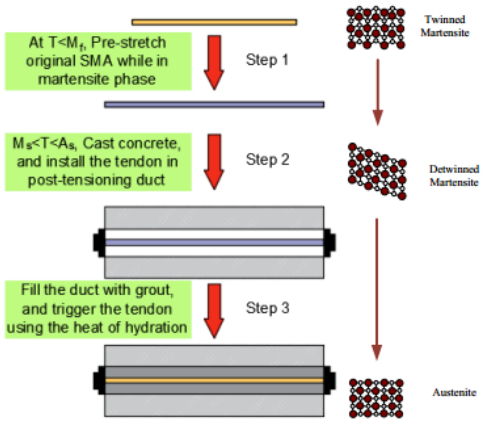

Figure 20. The process of self-post-tensioning using NiTiNb SMA wires [17].

Table 1. Temperature increase due to the heat of hydration of different grouts [17].

Specimen	Grout	Water-Grout Ratio	Initial Temperature (ºC)	Maximum Temperature (ºC)	Temperature Increase (ºC)
S1	Euclid	0.25	21	41	20
S2	Euclid	0.25	22	41	19
S3	Euclid	0.25	21	41	20
S4	Sika	0.24	21	48	27
S5	Sika	0.24	22	53	31
S6	Sika	0.24	21	48	27
S7	Five Star	0.25	22	41	19
S8	Five Star	0.25	22	41	19
S9	MasterFlow	0.27	22	41	19
S10	MasterFlow	0.27	22	41	19
S11	MasterFlow	0.32	22	40	18
S12	MasterFlow	0.32	22	40	18

Song et al. (2006) [26] used the SME of NiTi SMA wires to post-tension concrete specimens by using the recovery stress generated due to heating. At first, the change in resistance of the NiTi wires due to loading was used to measure the strain distribution in the concrete specimens without the help of any other external sensors. Three-point bending tests (Figure 21a) were carried out on concrete beam specimens of size 13.5 in. x 6 in. x 2 in. infused with NiTi wires of 0.015 in. diameter. Subsequently, the macro-sized cracks were closed using the post-tensioning force generated due to the shape recovery of the NiTi wires It was concluded that structures affected by explosions and earthquakes can be rehabilitated by heating the SMA externally so that the wires undergo shape recovery to reduce the macro-sized cracks (Figure 21b).

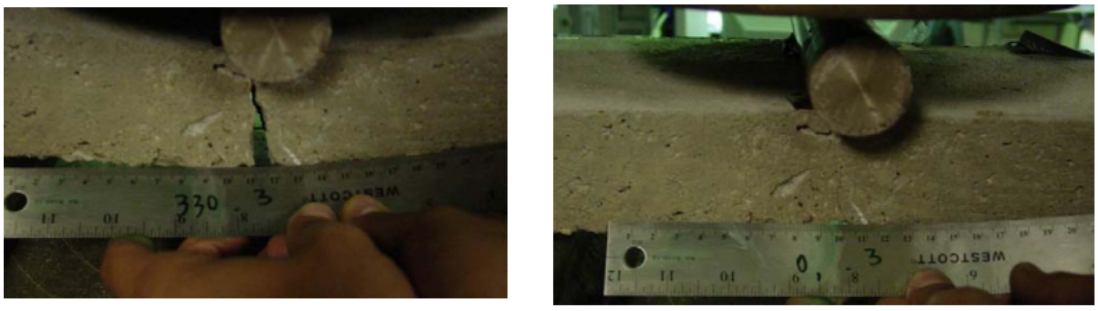

Figure 21. Shape recovery of NiTi infused concrete specimens: (a) after cracking; and (b) after shape recovery of NiTi wires [26].

The feasibility of using the SME of iron-based SMA (Fe-SMA) strips in place of CFRP strips for the prestressed strengthening of concrete structures was studied by Czaderski et al. (2014) [18]. The recovery stress of Fe-SMA varied between 250 to 300 MPa, which was relatively lower than that of NiTiNb SMA. The benefit of pre-stressing with Fe-SMA is the lower material cost and higher elastic stiffness. In this experiment, the prestressing was done by embedding the prestrained Fe-SMA in the concrete blocks and heating the SMA to induce recovery stress. The Fe-SMA strips were able to transfer a 3 MPa prestress when they were recovered. Lap-shear experiments (Figure 22) were conducted to study the bond behavior of the strips. The failure mode for ribbed Fe-SMA glued with cement-based mortar was compared to that of flat Fe-SMA without ribs and CFRP strips. It was observed that the failure in ribbed Fe-SMA was along the free length of the strip while the failure mode in flat Fe-SMA having no ribs and CFRP was sliding of the strip. Thus, it can be concluded that it is feasible to use ribbed Fe-SMA for the strengthening of concrete sections. However, CFRP strips with a cement-based mortar and Fe-SMA having no ribs cannot be used for strengthening application because of their poor bond quality.

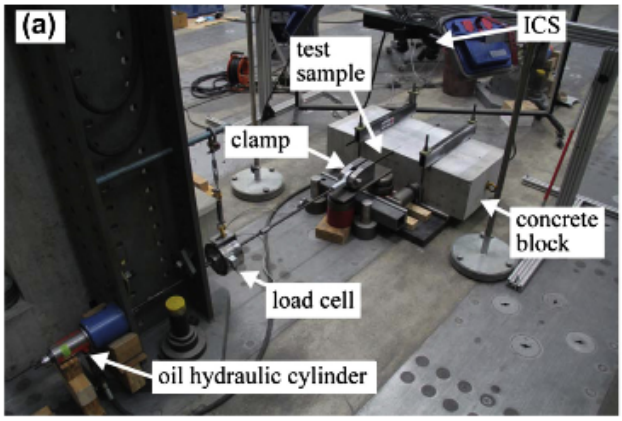

Figure 22. Test setup for lap shear test [18].

Applications Utilizing Superelasticity

The superelastic NiTi SMA restrainers were used as reinforcement for bridge decks to avoid excessive movement and unseating of the bridge girders during cyclic loadings (e.g., earthquakes). Andrawes et al. (2005) [10] conducted a nonlinear dynamic analysis of a typical California multiple-frame reinforced concrete box girder bridge using a suite of 10 ground motion records. A comparison of performances was made using different models of both superelastic SMA restrainers and the traditional steel cable restrainers. The superelastic restrainers reduced the relative hinge displacements significantly more than the steel restrainers. The average maximum hinge opening was reduced by up to 43% for superelastic restrainers, whereas the steel restrainers reduced the hinge displacement by only 16%. The reduction in hinge opening is attributed to the high elastic strains of the superelastic elements. The superelastic restrainers also displayed significant damping characteristics. The steel restrainers performed inadequately in most cases due to their low elastic strain limit. The study showed similar behavior in both the steel and superelastic restrainers during the first few cycles, but after the steel restrainers yield, residual strain accumulates in the steel whereas the superelastic restrainers have a re-centering ability and can recover the original length after being deformed at a strain between 6-8%. It was also observed that the maximum frame drifts did not depend on the type of restrainers.

A study was conducted by Ozbulut et al. (2016) [15] where these NiTi multistrand cables (Figure 23) were subjected to the uniaxial tensile test under various cyclic amplitudes and loading frequencies. The performance of the cables was evaluated in terms of energy dissipation, viscous damping, secant stiffness and residual strain. The cables consisted of 7 strands of wires each having an outer diameter of 8 mm and a length of 150 mm. The test setup is shown in Figure 24. The dissipated energy increased steadily with the increasing strain amplitude up to 7.2% (Figure 25a). The viscous damping first increased and then

became constant, but a small decrease was observed when some of the strands in the cable broke (Figure 25b). The secant stiffness decreased with the increase in strain amplitude (Figure 25c). For 100 loading cycles, the maximum residual strain was found to be 1.1%. The dissipated energy decreased by 34% as the number of cycles increased. It was observed that after the 40th cycle, increasing the number of cycles did not affect the properties of the NiTi multistrand cable. The study also showed that the performance of the cable changed while varying the strain rate of loading. The change in performance occurred because the higher rate of loading did not allow the latent heat from the wires to dissipate into the atmosphere, thus changing their transformation temperatures.

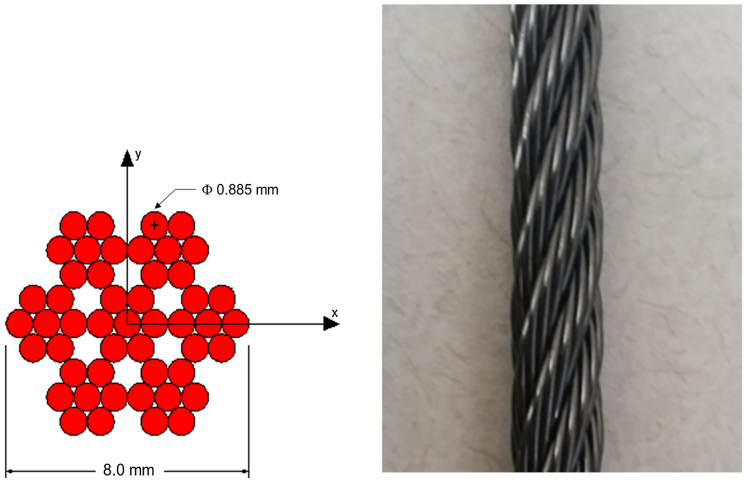

(a) (b)

Figure 23.Different views of multistrand NiTi cables: (a) cross-sectional view; and (b) longitudinal view [15].

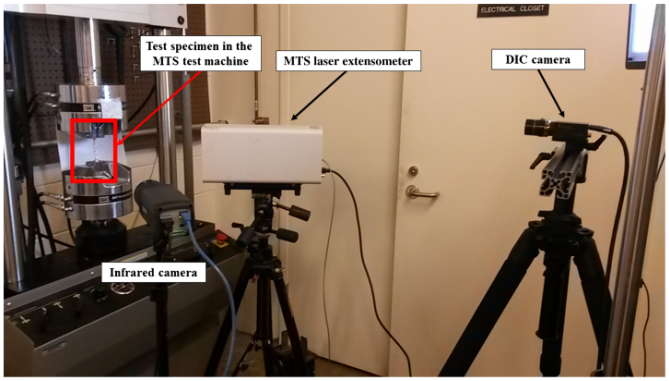

Figure 24. Test setup consisting of laser extensometer, DIC camera and infrared camera [15].

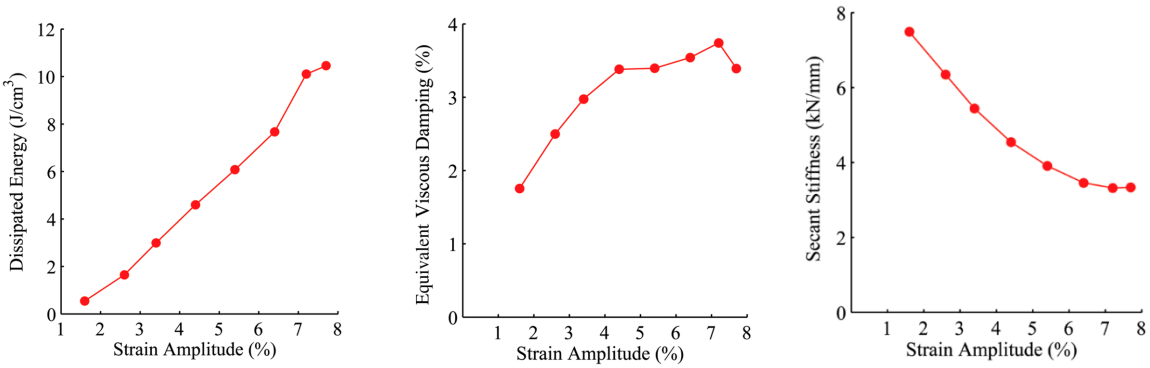

(a) (b) (c)

Figure 25. Variation of: (a) dissipated energy; (b) equivalent viscous damping; and (c) secant stiffness with strain amplitude [15].

The feasibility of using NiTi SMA wires as longitudinal reinforcement to reduce residual deflections by using their superelastic property was studied by Czaderski et al. (2006) [29]. SMA wires of 4 mm diameter were used to reinforce a 1.14 m long concrete beam. Tensile tests at different temperatures indicated that the Young's modulus in the martensite phase is 3.5 times lower than in the austenite phase. Subsequently, pullout tests were conducted on the wires to determine their bond strengths. Results indicated that different surface conditioning techniques (such as sandblasting) provide better bonding capability of the wires. Finally, four-point bending tests were performed on concrete beams reinforced with NiTi wires (Figure 26) and concrete beams without NiTi wires. The four-point bending test results showed that stiffness and yield strength of concrete beam reinforced with NiTi was noticeably higher in the austenite phase than martensite. The beams reinforced with NiTi wires were subjected to several deformation cycles to study the crack patterns. The stiffness of the beams decreased after deformation cycle 2 and a maximum crack width of 1.1 mm was measured during the 2nd and 4th cycle. Brittle fracture occurred at the mid-span of one of the NiTi wires during the 7th cycle. Finally, after the 8th cycle, the beam failed due to the brittle fracture of two NiTi wires. The reason for brittle failure of wires was fatigue corrosion cracking resulting from cyclic loading in presence of water and chlorides of the epoxy adhesive which was used for bonding the wires and concrete.

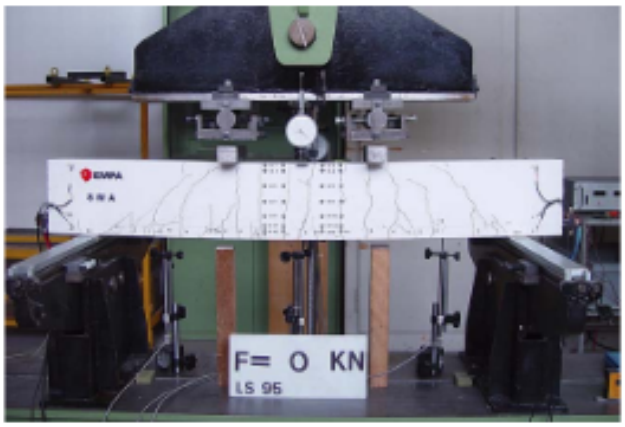

Figure 26. Four-point bending setup [29].

Saiidi et al. (2007) [19] used NiTi as tensile reinforcement in concrete beams and studied their effectiveness in reducing the permanent deformation in the beams by using their superelasticity. In this study eight (8) beams were designed and tested, out of which four beams were reinforced with NiTi wires and the other four were reinforced with conventional steel. In addition to this, analytical studies were also conducted on four beams of size 5 ft. x 5 in. x 6 in. with a combination of high strength steel and NiTi wires, and CFRP and NiTi wires. The beams were subject to four-point loading and designed to fail in flexure. The ratio of residual displacement to maximum displacement for the beams having NiTi wires as longitudinal reinforcement was 0.0333, whereas the beams with mild steel reinforcement had a ratio of 0.338. The NiTi reinforcement reduced the residual displacement by 90% when compared to the mild steel (Figure 27). The measured residual strain was 7% of the maximum strain for the beams reinforced with NiTi wires, and 85% of the maximum strain for the beams reinforced with steel. Due to the low modulus of elasticity of the NiTi wire, however, the stiffness of SMA reinforced beams were lower by 38%. The analytical test results on the SMA-mild steel reinforced beams showed an increase in stiffness (by up to 25%) over SMA reinforced beams with the ability to recover deformations partially.

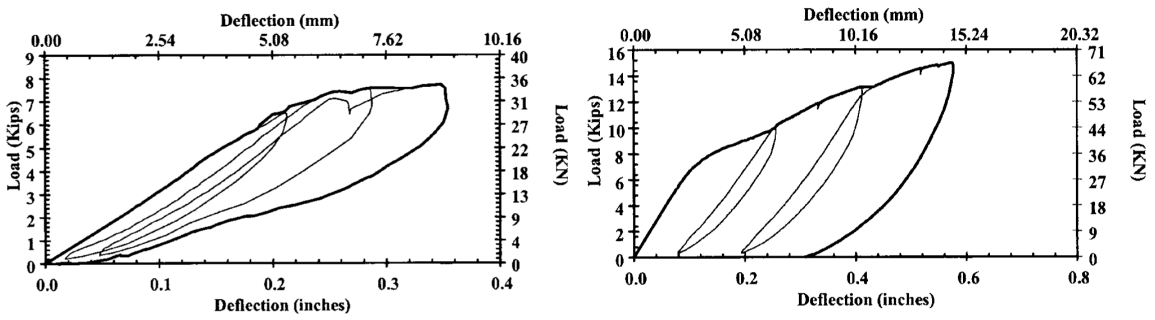

(a) (b)

Figure 27. Load vs. Deflection curve of: (a) NiTi SMA reinforced; and (b) mild steel reinforced beam [19].

The superelastic property of SMA has also been used to repair and strengthen heritage structures with architectural significance. For example, Indirli and Castellano (2000) [20] used the superelasticity of a system of pre-tensioned NiTi SMA rods connected in series with steel bars to restrain horizontal movement of a bell tower which was heavily damaged during an earthquake in Trignano, Italy in1996.

A study of slender heritage buildings, where superelastic NiTi SMA tie bars have been installed to resist excessive deformation and prevent collapse, was carried out by the same research group. The NiTi tie bars, which ran throughout the height of the tower, were anchored at the foundation. The tie bars were used to retrofit and rehabilitate the S. Giorgio Church Bell Tower which was severely damaged in a previous earthquake in 1996. This structure was declared intact after a subsequent earthquake in 2000 [20].

Song et al. (2006) [26] reviewed the application of SMA as actuators, passive energy dissipaters and dampers. They also studied the application of SMA as structural rehabilitators in smart structures. Over the years, many different materials like gold, cadmium and iron-based alloys have been used for their SME. Out of these, the best thermomechanical and thermoelectrical properties were exhibited by the NiTiNb SMA. The damping behavior of SMA depended on the factors like temperature, loading frequency and the number of loading cycles. It was also observed that the pre-strained martensitic NiTiNb had better damping capacity than NiTiNb SMA in the austenite phase. The dissipation of energy was dependent directly on the diameter of the wire and the effect of ambient temperature was negligible.

The SMA wires show damping property in tension as well as bending by their superelasticity. The SMA wires can be used in ground isolation systems, where isolators made of NiTi SMA wires can be installed at the junction of ground and superstructure to filter the seismic energy transferred from the ground and restore the structure to its original position. Both martensitic and superelastic NiTi wires can facilitate energy dissipation mechanisms when infused in structural elements because the wires are able to absorb the

vibration due to their hysteretic stress-strain relationship. The martensitic NiTi wires have a better damping capacity as compared to the superelastic SMAs but they must be externally heated to regain their original shape whereas the superelastic SMA, although having a lower damping capacity, has a strong re-centering property which results in lower residual strains. Figure 28 shows the use of superelastic NiTi SMA wires used in isolating systems by different researchers [22].

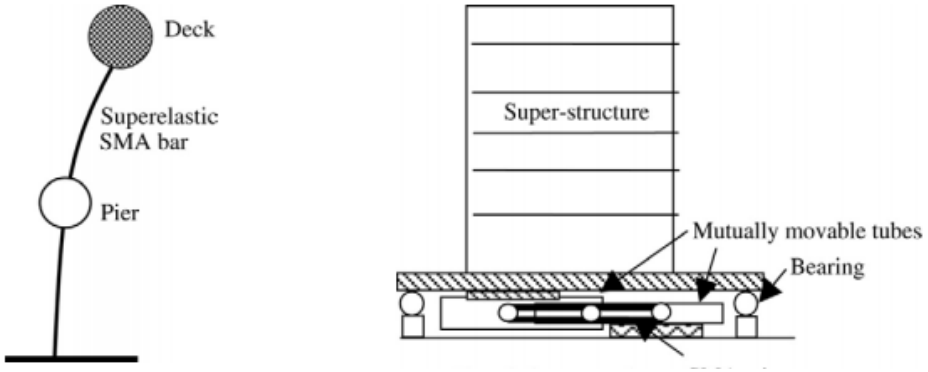

(a) (b)

Figure 28. Base isolation techniques by: (a) Wilde et al [22]; and (b) Dolce et al. [23].

Feasibility of using base isolating systems made of NiTi SMA bars exhibiting superelastic property was investigated for elevated highway bridges by Wilde et al. (2000) [22]. It was observed that the excitation level had a substantial effect on the effectiveness of the base isolation system. At small excitation levels, a system of NiTi bars firmly link the pier and the deck slab but at medium excitation, stress-induced forward transformation leads to a relative displacement between the pier and bridge deck. At high loading state, the SMA behaves superelastically, and there were minimal displacements observed when compared to ordinary damping systems.

A NiTi-based isolation system was investigated for its load carrying capabilities. Dolce et al. (2001) [23] found that the isolation system can carry 600 KN force and withstand up to 180 mm deflection. The NiTi wires were wound around three stubs connected to tubes, which allowed reciprocal movement between the substructure and the superstructure. The system was very effective in filtering energy transmission. The feasibility of using the NiTi-based base isolation system as a re-centering isolation system was thus verified.

Casciati et al. (1998) [24] used finite element method to analyze static and dynamic responses of bridges to earthquakes which have been retrofitted with martensitic NiTi bars. The result of such simulations verifies the feasibility of using NiTi SMA as damping elements for bridges. The techniques of application of NiTi in different types of bridges are shown in Figure 29.

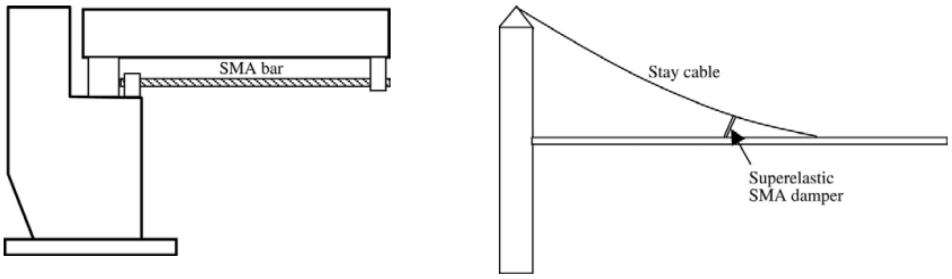

Figure 29. NiTi SMA bars used as damping element for bridges [24].

Anchorage made of NiTi SMA rods have been used as vibration dampeners in connections between beam-columns and other parts of the structures as shown in Figure 30. Tamai et al. (2003) [21, 30] found that anchorages made using NiTi rods of 20-30 mm diameter improved the response of the joints during seismic ground motion. Results obtained from numerical simulation of these connections subject to pulsating tension loading tests show that the connections have a good capability of dissipating energy and reducing vibration under severe ground motions.

Martensitic NiTi tendons were used as primary load transferring elements in structures by Leon et al. (2001) [22]. The tendons achieved 4% repeatable hysteresis in rotation and sustained a strain up to 5% without incurring any permanent damage.

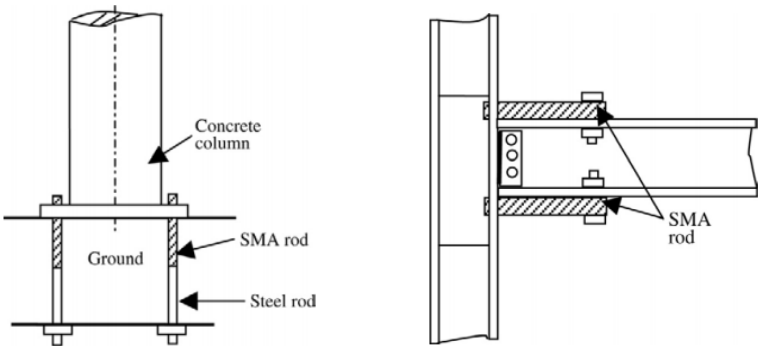

Figure 30. SMA used as connectors between structural members [30].

Superelastic SMA wires have been used for shape restoration of concrete beams by Sakai et al. (2003) [25]. The results of this study indicated that mortar beams reinforced with NiTi SMA wires could recover their shape entirely even after developing substantial cracks and deflection. Superelastic restoration of multistrand NiTi SMA cables was used to close cracks in concrete beams (Figure 31a) after being loaded to 11000 lbf and developing significant cracks. Fourteen (14) multistrand NiTi cables of 0.125 in. diameter with 2% prestrain were used to achieve post-tensioning of a 2 ft. long concrete beam with a cross section 4 in. x 6 in. The cables were restrained at both ends with a special type of clamps. The cables developed

post-tensioning forces due to their superelastic property when the applied load was removed. After the specimen cracked at 11000 lbf load the cracks were closed by the NiTi cables as shown in Figure 31b [25].

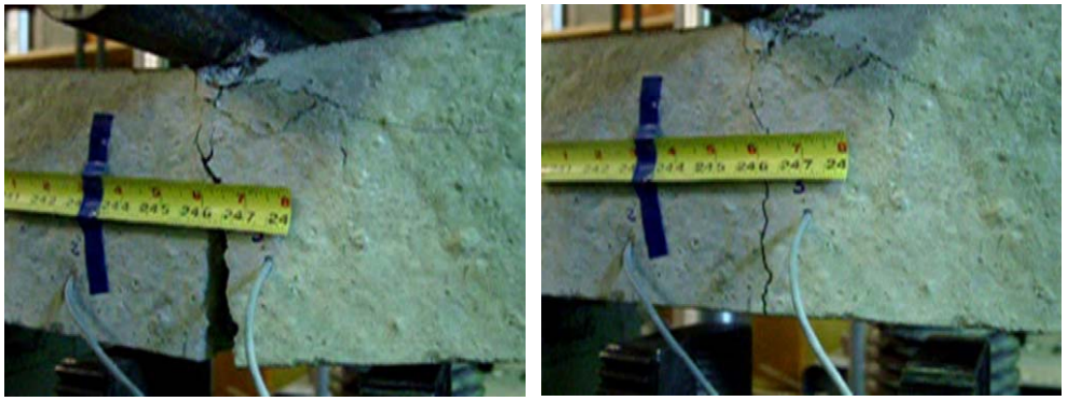

Figure 31. Elastic restoration of concrete beam: (a) cracking of the beam; and (b) restoration of the crack. [25].

Bond Characteristics of SMA with concrete

The bond between SMA wires or bars and concrete is of paramount importance when anchorage is not provided. Characterization of the bond between SMAs and concrete are summarized in this section.

Billah and Alam (2016) [27] conducted various experiments to study the bond characteristics between NiTi SMA bars and concrete. The change in bond behavior with the variation of parameters such as bar diameter, concrete strength, bonded length, concrete cover and surface treatment (sand coating) were studied by the authors. Several cylindrical concrete samples were prepared with a 450 mm long, 0.75% prestrained NiTi bar embedded at the center. The samples were subjected to pushout tests under varying testing parameters, as shown in Figure 32. For smooth NiTi bars, the stress increased elastically up to a peak load after which the bond failed. The unloading portion of the curve descended linearly until it reached a residual stress and remained constant beyond that. The slip was negligible during the loading phase and started to increase after the sample cracked during the unloading phase and large slippage was observed as the sample reached its residual load level (Figure 33). The smooth bars failed without any splitting crack indicating that there was no significant bond between smooth bars and concrete. The average residual bond strength of a NiTi bar coated with 600 μm sand was 29% and 35% higher than a bar coated with 300 μm sand, and a smooth bar respectively. Test results also indicated that the average maximum and average residual bond strength decreased with the increase in embedment length. The bond strength increased with the increase in strength of concrete. The average maximum bond strength

decreased with the increase in bar diameter, whereas the residual bond strength remained quite unchanged.

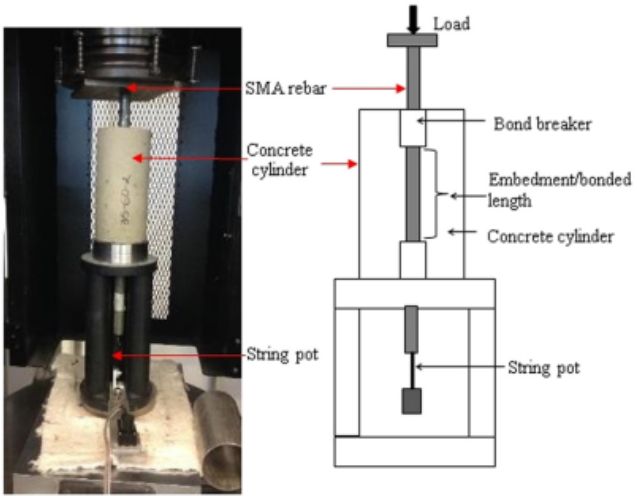

Figure 32. Test setup of the push-out test [27].

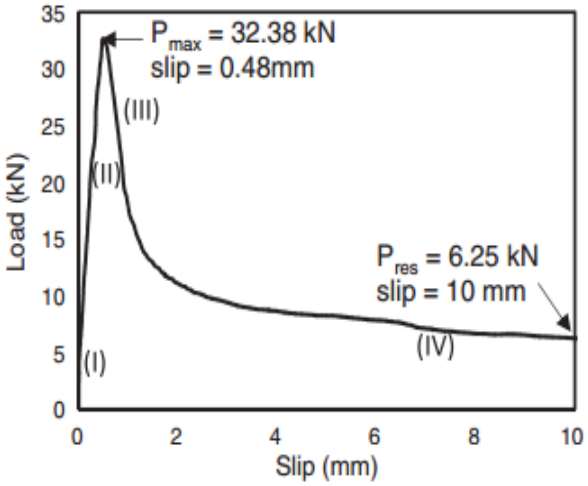

Figure 33. Load vs. Slip curve for smooth NiTi SMA bars [27].

The effect of various parameters such as surface conditioning (sandblasting), bar diameter, embedment length and anchorage on the effectiveness of the NSM NiTi SMA bars, used in strengthening applications, was studied by Daghash et al. (2017) [28]. For this experiment, a C-shaped cube concrete specimen of size 305 mm and average compressive strength 38 MPa was made with a groove equivalent to twice the diameter of the bars (Figure 34a). The specimens were subjected to a pull-out test at a constant displacement rate as shown in Figure 34b. The test results were interpreted based on average bond stress and the stress-slip curves of different samples. Sandblasting was found to be an effective surface treatment

technique which increased the average maximum bond strength. The increase in surface roughness improved the mechanical interlock between the bar and the epoxy resulting in increased bond strength. The bond strength decreased with the increase in bar diameter and bond length. The bond strength first increased with the increase in bond length for up to 7 times the diameter of the bar and then started to decrease. This happens due to the change in failure mode from epoxy splitting to gradual bar slippage at peak stresses. The difference in slippage between the loaded and unloaded ends of the bar at peak stresses is caused due to the change in failure mode. Moreover, providing end hooks also gave significant mechanical anchorage to the NiTi bars and increased the average bond strength by almost 33%.

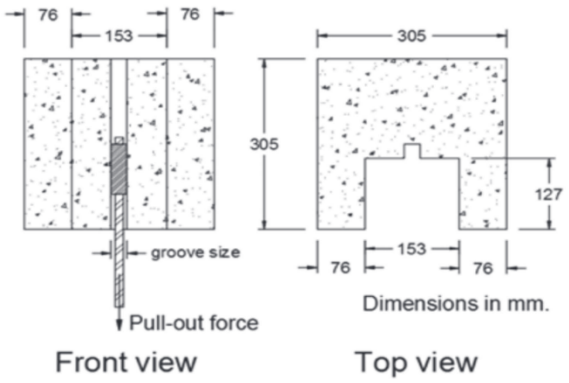

(a)

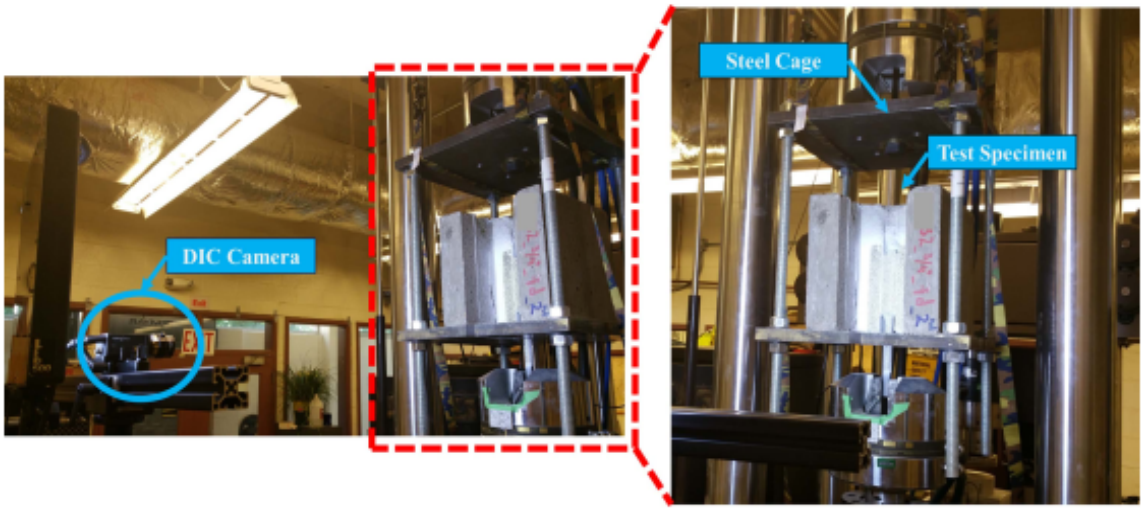

(b)

Figure 34. Pullout test: (a) specimen details; and (b) test setup [28].

OBJECTIVE

This work seeks to verify the feasibility of using heat-induced post-tensioning via NSM SMA in existing cracked reinforced concrete girders (Figure 35). In this study a NiTiNb alloy was evaluated for feasibility in post-tensioning of existing bridge girders without the conventionally experienced problems with anchorages, high construction costs, long lane closure times, long construction times, etc.

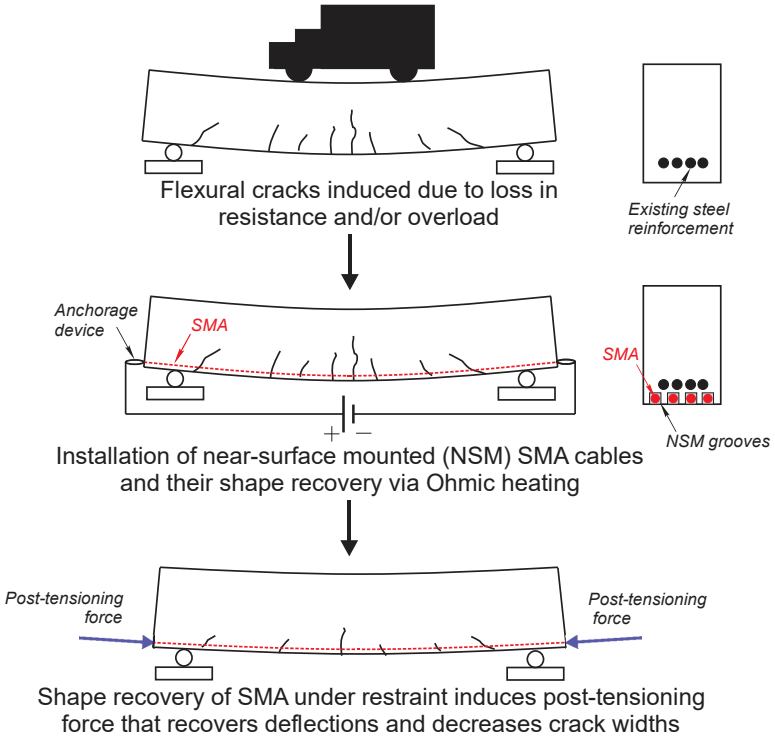

Figure 35. Concept of reinforced concrete girder post-tensioning with NSM NiTiNb.

SCOPE

The feasibility of utilizing SMAs for post-tensioning was evaluated through a series of material characterization tests on NiTiNb wires, bond characterization tests on plain concrete beams reinforced with NiTiNb and post-tensioning as well as flexural tests on reinforced concrete girders. The following specific experiments were performed:

1. Tensile tests on NiTiNb wires in austenite phase to determine the material's stress-strain behavior.
2. Restrained recovery tests on NiTiNb wires via Ohmic heating to determine the recovery stress and the potential post-tensioning force.
3. Bond characterization tests on plain concrete beams to assess the quality of the bond between the NiTiNb wire and the grouting material.
4. Post-tensioning tests on cracked reinforced concrete girders to verify the feasibility of the post-tensioning technique on structural-scale girders.
5. Four-point flexural tests on post-tensioned girders to observe the strengthening of the girders because of post-tensioning.

METHODOLOGY

The experimental program included four types of experiments: (1) tensile tests and restrained recovery tests on NiTiNb wires; (2) bond characterization tests on plain concrete beam specimens reinforced with NiTiNb wires; (3) post-tensioning tests on cracked reinforced concrete girders; and (4) four-point flexural tests on post-tensioned girders.

Overview of Experimental Program

Tensile Tests on NiTiNb Wires

Tensile tests were conducted on NiTiNb in austenite phase to obtain the stress-strain response of the material in its high-stiffness phase, following phase transformation. In addition, to quantify the prestressing potential of the NiTiNb, the recovery tests were conducted on restrained SMA to obtain the recovery stress.

Table 2. Summary of tensile tests on NiTiNb.

Type of test	No. of replicates
Tensile test on austenite	3
Restrained recovery test	3

Bond Characterization Tests on Plain Concrete Specimens

Following the material characterization of NiTiNb wires, bond characterization tests were performed on multiple types of plain concrete beam specimens to characterize the quality of bond between the near-surface mounted NiTiNb wire and the grouting materials. The test specimen consisted of a 14 in. x 4 in. x 4 in. plain concrete beam with a 0.1 in. notch at midspan to simulate cracked concrete (Figure 36). Near-surface mounted (NSM) NiTiNb wire is placed in the longitudinal groove to serve as main tensile reinforcement. A portion of the NiTiNb wire was debonded and embedded in the grout to avoid the effects of compressive stress at the supports on the NiTiNb bond performance. Conditions of the middle portion of the groove were varied and kept as a test variable. In addition, anchorage device used at the ends of the specimen was also another test variable.

The experimental program was designed to evaluate the effects of different test variables on the specimen strength, to help determine the bond characteristics of the NiTiNb wire with the grouting material. The most favorable conditions for successful transfer of the post-tensioning force to the reinforced concrete girder were also decided based on the results of

the bond characterization tests. The variables included: specimens post-tensioned with NiTiNb wire (PT) vs. specimens reinforced with austenite (AU); specimens with middle portion of NiTiNb bonded *before* NiTiNb recovery (BOB) (hatched area of the groove in Figure 36 filled with grout) vs. unbonded NiTiNb wire (UB) (hatched area of the groove in Figure 36 left unfilled) vs. specimens with middle portion of NiTiNb bonded *after* NiTiNb recovery (BOA) (hatched area of the groove in Figure 36 filled with grout); specimens with anchoring device (A) vs specimens without anchoring device (N). Specimen nomenclature was adopted based on the described variables. Summary of all test specimens is provided in Table 3.

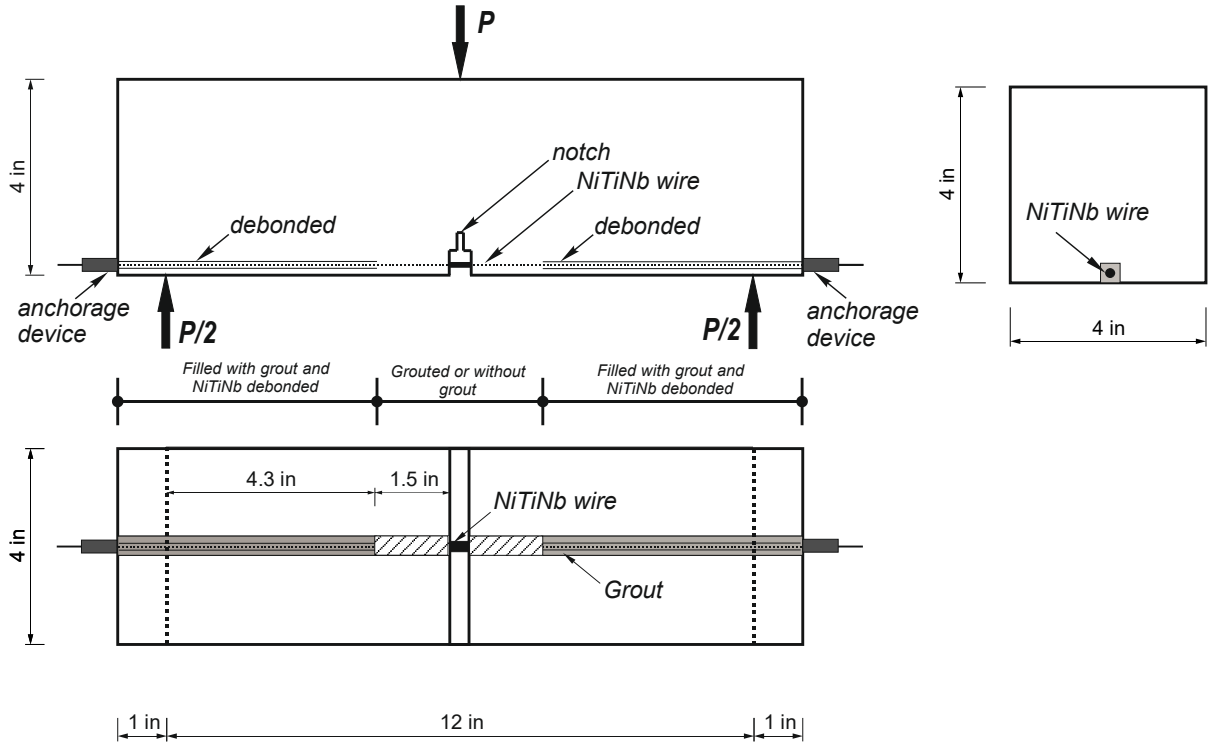

Figure 36. Bond characterization test method schematic.

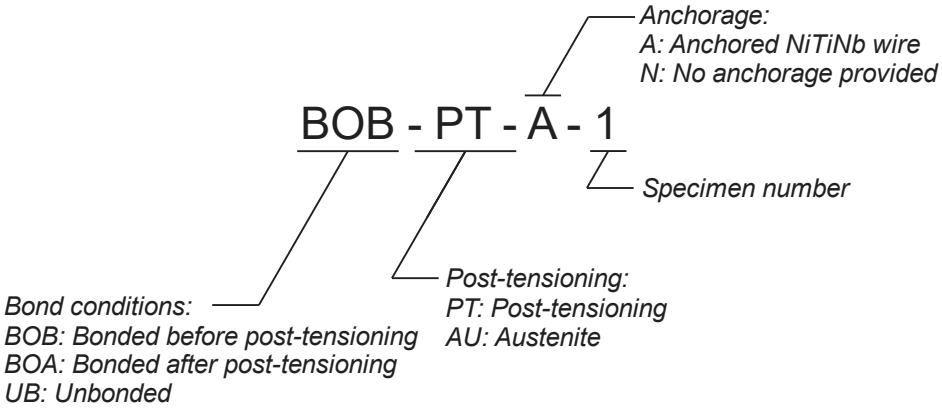

Figure 37. Specimen nomenclature.

Table 3. Summary of bond characterization test specimens.

Specimen
Control-1 (plain concrete) Control-2 (plain concrete)
BOB-AU-N-1 BOB-AU-N-2
BOB-PT-N-1 BOB-PT-N-2 BOB-PT-N-3
BOB-PT-A-1 BOB-PT-A-2
UB-PT-A-1 UB-PT-A-2
BOA-PT-A-1

Tests on Reinforced Concrete Girders

Reinforced concrete girders measuring 7.5 ft. in length and having a cross section of 9 in. x 16 in. were tested to evaluate the feasibility of the proposed post-tensioning technique in a structural-scale girder. The tests were carried out in three stages: (1) loading of the girders in stages to develop cracks and residual midspan deflection; (2) post-tensioning of the cracked girders via Ohmic heating of the NiTiNb wires; and (3) loading of the post-tensioned girders in stages up to failure. A control specimen without NiTiNb wires was first loaded up to failure to assess the behavior of the girder without post-tensioning with the NiTiNb wires. All the girders had similar longitudinal and transverse steel reinforcement and were prepared with the same batch of concrete. The experiments were performed by keeping the number of NiTiNb wires in each of the girders as a test variable. Summary of the reinforced concrete girder test specimens is provided in Table 4.

Table 4. Summary of reinforced concrete girder test specimens.

Name of Specimens	Number of NiTiNb wires
Control	0
8-SMA	8
10-SMA	10
12-SMA	12

Materials

NiTiNb Wire

The SMA selected for this study was NiTiNb. The ternary alloy was selected over a more common binary NiTi due to its wide thermal hysteresis which makes it appropriate for the range of temperatures experienced by bridges. NiTiNb alloy 8-ft. wires measuring 0.154 in. (3.92 mm) in diameter were used in this study. The wires were supplied with a minimum 2.5% guaranteed prestrain. Per manufacturer, the material was reported to have a minimum A_s of 60 °C in the prestrained state. Transition temperatures, as reported by the manufacturer, are summarized in Table 5. The wires had a standard black oxide surface finish.

Table 5. DSC transformation temperatures at lead and tail of coil after annealing at 850 °C for 30 minutes, as per manufacturer.

Location on the coil	M_f	M_s	A_s	A_f
Lead	-79	-56	-18	6
Tail	-80	-59	-19	4

Concrete for Bond Characterization Test Specimens

Bond characterization specimens were made of concrete in which a water to cementitious material ratio (w/cm) of 0.37 was maintained. The concrete mixture was composed of: river sand, coarse aggregate with gradation curve #89, and Portland Cement Type I/II. No admixtures were used. Coarse aggregate moisture content was determined as per ASTM C566 [32], prior to mixing the concrete, to adjust the batch quantities. The moisture content of the coarse aggregate was found to be 8.60%. No pozzolans were included in the mix design. The final mix proportions are shown in Table 6. Average compressive strengths at 7

and 28 days obtained from 4 in. x 8 in. concrete cylinders (ASTM C39 [33]) were respectively 6600 psi and 8000 psi.

Table 6. Concrete mix design.

MATERIAL	SOURCE	WT. PER YD^3 (LB)	SPECIFIC GRAVITY	VOL. PER YD^3 (CF)	WT. PER BATCH (LB)	ADJ. WT. PER BATCH (LB)
CEMENT	Holcim	871.8	3.15	4.43	248.6	248.6
WATER	Local	340.0	1.00	5.45	92.7	76.1
FINE AGG.	River Sand	930.0	2.460	6.06	265.2	259.0
COARSE AGG.	#89	1356.3	2.300	9.45	386.8	409.6
AIR (DESIGN)	Local	0.0		1.620		
TOTAL		3498.02		27.00		

Concrete for Reinforced Concrete Girder Test Specimens

Casting of the reinforced concrete girders was done using ready-mix concrete which was delivered by Barry Concrete, Inc. The mixed design for a concrete of target strength 3500 psi was performed by Barry Concrete, Inc. The water to cementitious material ratio (w/cm) of the mix was 0.49. A mixture of Ash Grove Type I/II Portland Cement and Type C Fly Ash (3:1 by weight) was used as cementitious material. A mixture of Grade A gravel (conforming to ASTM C33 [34]) and pea gravel was used as coarse aggregate. River sand (conforming to ASTM C33 [34]) was used as fine aggregate. A water-reducing admixture (Sikament 686) was used to maintain the workability of the fresh concrete while reducing the demand for water in the mix. An air-entraining admixture (SikaAir 2100) was used to maintain good workability and to prevent segregation and bleeding of the fresh concrete. The moisture content of the coarse aggregate and the fine aggregate was assumed to be 1% and 4%, respectively. The weights of the different components were adjusted accordingly to account for the moisture content of the aggregates. The final mix proportions are shown in Table 7. Average compressive strengths at 7 and 28 days, obtained from the 4 in. x 8 in. concrete

cylinders (ASTM C39 [33]), were 3500 psi and 5026 psi respectively. Three-point bending tests (per ASTM C78 [35]) on plain concrete bond characterization specimens showed that the flexural strength of concrete to be 530 psi.

Table 7. Concrete mix design.

MATERIAL	SOURCE	SPECIFIC GRAVITY	VOL. PER YD^3 (CF)	WT. PER BATCH (LB)	ADJ. WT. PER BATCH (LB)
CEMENT	Ash Grove	3.15	1.80	353	353
FLYASH	ISG	2.65	0.70	117	117
WATER	Local	1.00	3.69	230	166
FINE AGG. (SAND)	Grangeville	2.62	7.56	1235	1284
COARSE AGG. (GRADE A GRAVEL)	Grangeville	2.59	9.38	1481	1496
COARSE AGG. (PEA GRAVEL)	Grangeville	2.60	2.53	400	404
AIR (DESIGN)	Local		1.35	1.17	1.17
TOTAL			27.00		

Steel Reinforcement for Reinforced Concrete Girders

The longitudinal reinforcement consisted of #4 deformed bar and the stirrups were made of #3 deformed bar. The steel bars were Grade 60 conforming to ASTM A615 [36] as per the material testing report provided by the supplier. The mill test certificate for the steel bars indicated a yield stress of 69 ksi and a tensile strength of 107 ksi.

Specimen Preparation

Tensile Test Specimens

Six 11-in. SMA wires cut from the 8-ft. wire supplied by the manufacturer. Three specimens used for characterization of the tensile properties of austenite were heated above A_f via Ohmic heating by passing current of approximately 44 A until the temperature of the wire reached 200 °C. The heating-initiated shape recovery and consequent transformation from martensite to austenite. Once the specimens cooled down to room temperature, strain gages were attached to the surface of the wire. The remaining three specimens were used for the recovery test on NiTiNb and required no special preparation.

Bond Characterization Test Specimens

Concrete Casting. Plain concrete beam specimens were cast for bond characterization tests. Fine aggregate (sand) was oven-dried for 24 hours to minimize the absorbed moisture. Coarse aggregate was soaked in water for at least 24 hours to saturate at the time of mixing. Concrete was mixed in a portable mixer. Coarse aggregate, sand and cement were added to the mixer first. Dry ingredients were mixed for 3-5 minutes before adding water into the mix. Water was poured gradually to achieve uniform dispersion. Slump was measured according to ASTM C143 [37] and was found to be 4 in. The concrete air content of 4-5% was measured as per ASTM C231 [38].

Following mixing, concrete was immediately poured into aluminum-plywood forms as shown in Figure 38. The forms were coated with a form-release agent to facilitate specimen removal and cleaning of the forms. Concrete was poured half-way into the forms and vibrated for 30 seconds. Forms were fully filled and again vibrated for 30 seconds. Excessive concrete from the top surface was removed. The top surface was then levelled using a trowel (Figure 39). After filling the forms, concrete was allowed to harden for 24 hours before demolding. The specimens were cured in a curing tank in the lime solution according to ASTM C31 [39] for 28 days.

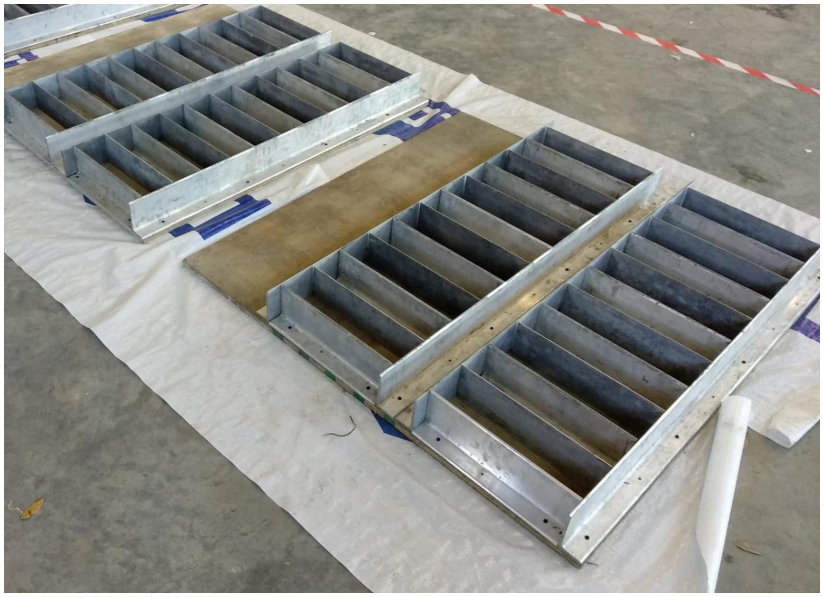

Figure 38. Aluminum-Plywood forms.

Figure 39. Forms filled with fresh concrete.

Beam Cutting. Following curing, the plain concrete beams were cut to introduce a 1 in. notch in the middle to simulate cracked concrete (per Figure 36). The thickness of the notch was approximately 1/8 in. The bottom ½ in. of the notch was widened to allow for placement of a strain gage on NiTiNb wire at the later stages of the test. A longitudinal groove measuring approximately 0.39 in. x 0.39 in. was introduced to facilitate the placement of NSM NiTiNb wire (Figure 40). A plain concrete beam with the notch and longitudinal groove is shown in Figure 41.

Figure 40. Saw-cutting of longitudinal groove.

Figure 41. Axonometric view (from the bottom) of a bond characterization specimen with 1-in notch and longitudinal groove.

Different types of specimens were prepared for testing, per Table 3. Debonded region, as indicated in Figure 36, was maintained by wrapping that portion of NiTiNb wire with tape. Debonded NiTiNb on each side of the notch was instrumented with a thermocouple to allow for temperature measurements; another thermocouple was installed within the notch region. The NiTiNb wire was then placed into the groove, and the debonded portion of the groove was filled with SikaQuick® VOH grout mixed with a latex admixture (SikaLatex® R) to enhance bonding between the grout and NiTiNb. The grout was allowed to cure for a minimum of 3 days (corresponding to grout compressive strength of 3000-4000 psi, per manufacturer) before testing the specimens. In the specimens with bonded NiTiNb wire, the

portion of the groove adjacent to the notch (hatched area in Figure 36) was also filled with the same grout. In specimens with unbonded NiTiNb, the wire was left exposed (Figure 43b).

Anchored specimens utilized the anchoring device consisting of strand chucks supported against the 1/8 in. thick steel plate resting on the concrete surface. Components of the strand chuck are: jaw segments, retaining ring, and the strand chuck body (Figure 44). The strand chuck body has a tapered hole which allows the jaw segments to slide in. While jaw segments are smooth on the outer surface, the inner diameter is populated with rows of fine ridges (also known as “teeth”). When the wire is placed between the jaw segments the jaw segment teeth bite into it preventing it from slipping. Retaining ring is used to keep the jaw segments together. Strand chuck components on one of the specimen ends are demonstrated in Figure 45.

Figure 42. NiTiNb wires prepared for placement in the grooves: Type K thermocouples’ probes were affixed to the wire surface followed by wrapping with scotch tape to provide debonded length.

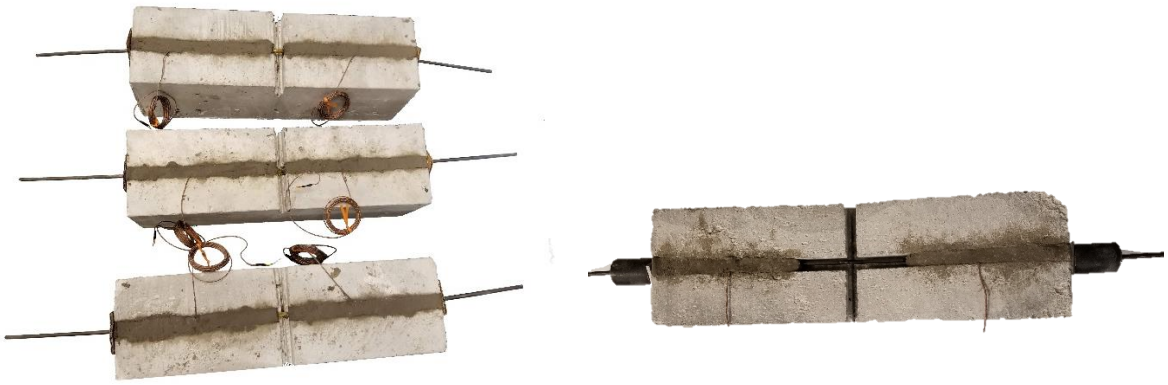

(a) (b)

Figure 43. Example of bond characterization specimens with: (a) bonded NiTiNb without anchorage; and (b) unbonded NiTiNb with anchorage.

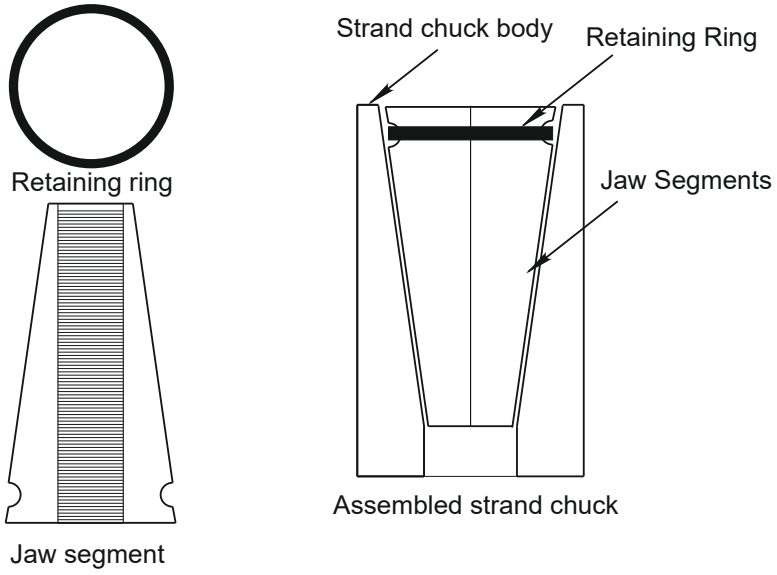

Figure 44. Strand chuck components.

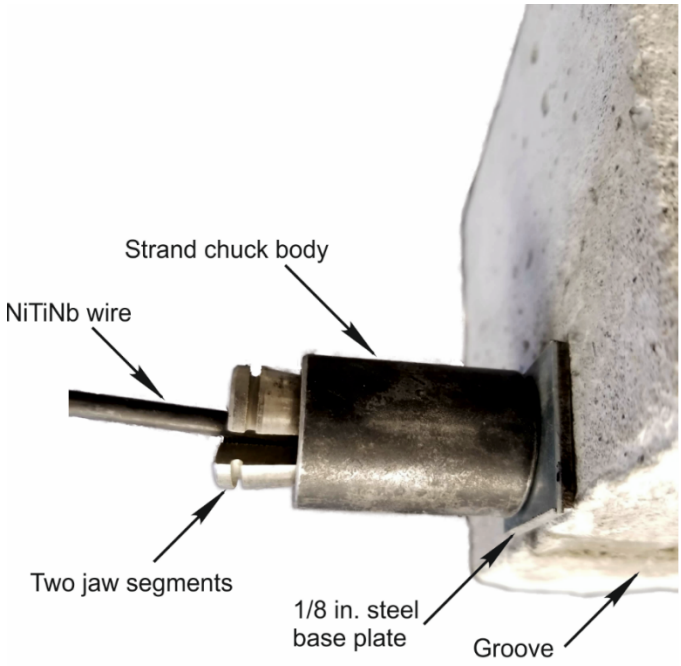

Figure 45. Components of the anchorage system utilizing strand chucks.

Reinforced Concrete Girder Test Specimens

Design. The reinforced concrete girder test specimens were designed to behave as a single-reinforced concrete beam according to ACI 318-14 [32]. The dimensions of the reinforced concrete girder specimens were fixed at 7.5 ft. x 16 in. x 9 in. The longitudinal tensile reinforcement consisted of 3-#4 steel bars. 2-#4 bars were provided on the top to hold the stirrups in place. Nineteen (19) 2-legged stirrups made of #3 bars were provided at a spacing of 4 in. from the support up to the start of the loading span. The design is shown in Figure 46.

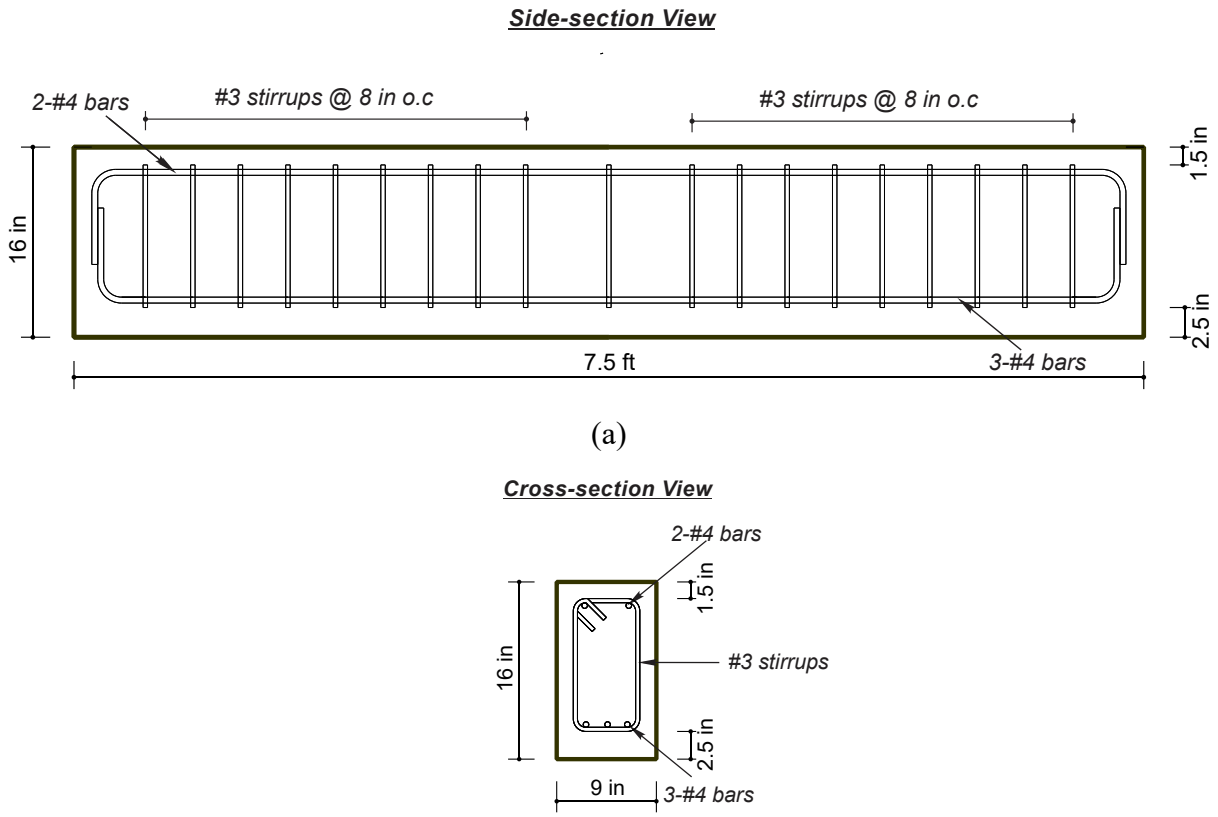

Figure 46. Design details of reinforced concrete girders: (a) side-section view; and (b) cross-section view.

Formwork. The formwork for the reinforced concrete girders were made of plywood sheets, wooden runners and cross braces as shown in Figure 47.

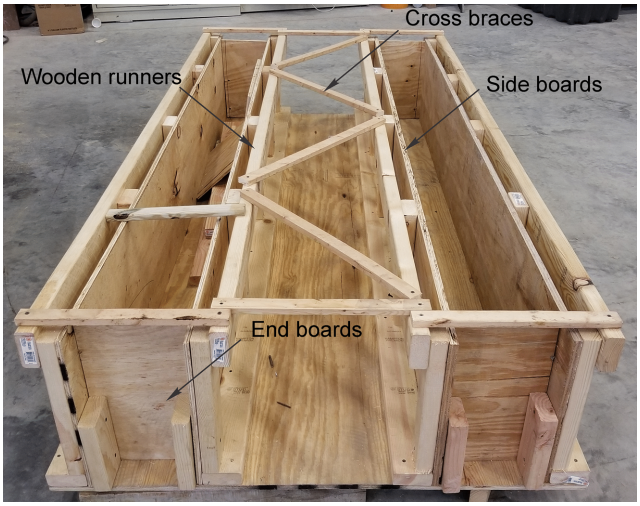

Figure 47. Formwork for casting of reinforced concrete girders.

Assembling Reinforcement Cages. After building the formwork, the reinforcement cages were assembled. The steel bars were cut and bent by the supplier according to the design drawings. Subsequently, the bars were delivered to the laboratory where they were assembled and placed in the forms. Lifting lugs were also attached to the top bars of the girders (on both the ends) to facilitate lifting and moving.

Figure 48. Assembled reinforcement cages.

Concrete Casting. Four (4) reinforced concrete girders measuring 7.5 ft. x 16 in. x 9 in. were cast for the post-tensioning and flexural tests. Prior to casting, plumbers putty was applied to seal any gaps in the formwork, thus preventing leakage of cement slurry during casting. Form releasing agent was applied on the inside surface of the forms to facilitate easy demolding. The reinforcement cages were placed inside the forms after attaching cover blocks on bottom and side of the cages to maintain the cover on all sides. The cover in the bottom of the girder was 2.5 in. and on the top and two sides was 1.5 in.

Figure 49. Reinforcement cages placed in the form.

The concrete was mixed and delivered in a transit mixture truck by Barry Concrete, Inc. The concrete was poured using a hose attached to a concrete pump (Figure 50). Slump of the fresh concrete, measured according to ASTM C143 [37], was 3.75 in. The air content of the mix was 2.5%, measured as per ASTM C23 [38]. During casting, the forms were filled halfway and vibrated using immersion vibrators to ensure proper compaction of the concrete. The forms were subsequently filled up to the top with concrete and vibrated a second time. The top surface of the girders were finished using straight edges and trowels (Figure 51). After the casting was completed, the girders were allowed to harden for 24 hours before demolding. The girders were cured for 10 days by spraying with water and covering with plastic sheets to minimize evaporation. After 10 days of curing, the girders were lifted off the base board and placed on concrete support blocks for subsequent stages of specimen preparation.

Figure 50. Concrete pumping arrangement.


(a)


(b)

Figure 51. Reinforced concrete girders: (a) during casting; and (b) after final setting and demolding.

Cutting Grooves in the Reinforced Concrete Girders. Grooves were introduced at the bottom surface of the girders to install the NiTiNb wires in the cover region. The various arrangements of the NiTiNb wires in the grooves are shown in Figure 52. First, the girders were flipped upside down. Then, the grooves were cut using a Metabo MFE40 wall chaser with two blades separated by a gap of 9 mm. The grooves were 40 mm deep, so that two NiTiNb wires can be accommodated in each groove along with the strand chucks at the ends of the girder. Each groove was wide enough (9 mm) to prevent friction between the wires

and the groove walls. During cutting, a portable vacuum cleaner was attached to the wall chaser to collect the dust to keep the work environment free from dust. The cut was made in two passes, each 20 mm deep, to reduce the wear of the blades (Figure 53a). The remaining concrete inside the grooves was chiseled out after cutting with the wall chaser. Pressurized water was used to expel the concrete debris from inside the grooves. The final cuts are shown in Figure 53b.

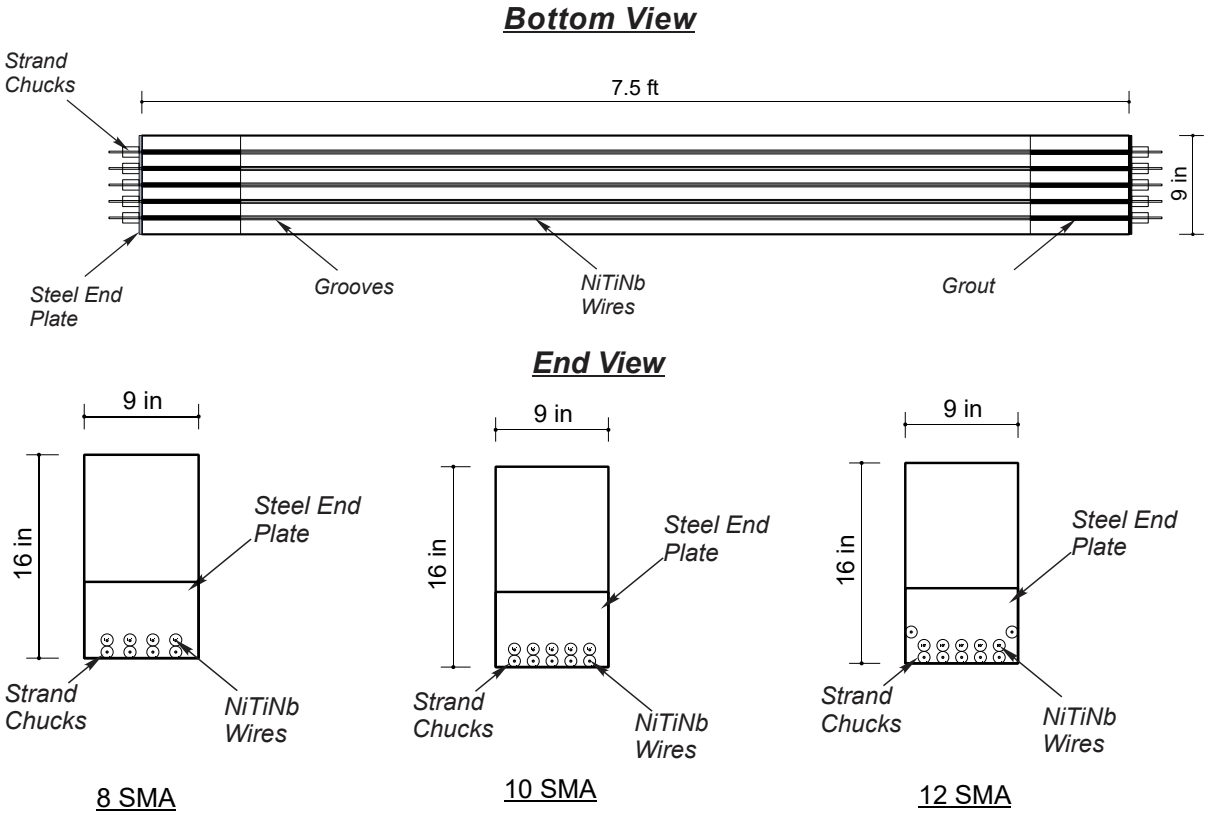

Figure 52. Arrangement of NiTiNb wires in different reinforced concrete girders: (a) bottom view; and (b) end view.

(a) (b)

Figure 53. Cutting groves in the cover region of the girders: (a) sawing with Metabo MFE40 Wall Chaser; and (b) a girder with grooves.

Grouting and Placing of the NiTiNb Wires in the Grooves. NiTiNb wires, measuring 0.154 in. (3.92 mm) in diameter and 8 ft. in length, were placed inside the grooves and kept unbonded throughout. 1/4 in. thick steel plates, measuring 9 in. x 6 in., were attached at the ends of the girders to ensure proper bearing of the strand chucks. To ensure adequate bearing surface at the supports, the grooves in the support region were filled with SikaQuick® VOH grout mixed with a latex admixture (SikaLatex® R) in a ratio of 44:7 (by weight) as prescribed by the manufacturer (Figure 54). NiTiNb wires at the support region were kept unbonded by placing them in polyvinyl chloride (PVC) tubes (Figure 54) before filling grooves with the grout.

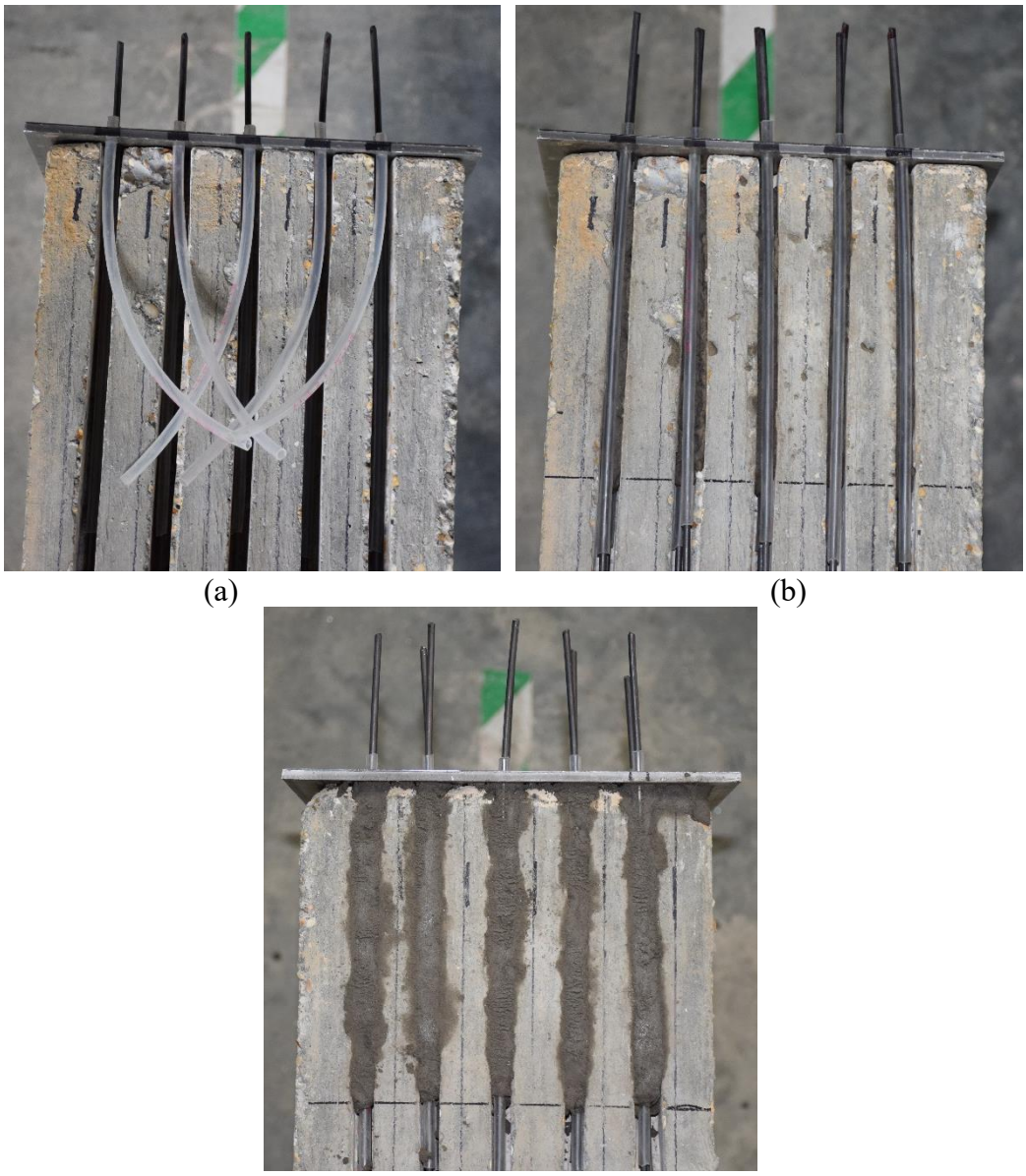

Figure 54. Different stages of placing NiTiNb wires in grooves: (a) first ‘layer’ of wires passed through PVC tubes placed inside each groove; (b) second ‘layer’ of wires passed through the PVC tubes; and (c) final grouting within the support region.

Experimental Procedures

Tensile Test

All tensile tests were performed on a 22-kip MTS universal testing machine.

Tensile Tests on Austenite. The specimens were placed in the testing machine using the hydraulic grips; the sample had a grip length of 2 in. and a total gage length of 6.5 in. A 2-in. extensometer was affixed to the specimen, in addition to the previously attached strain gage.

The experiments were performed under the constant displacement rate of 10 mm/min. The specimen was loaded until rupture. The load, cross-head displacement and strain data were recorded.

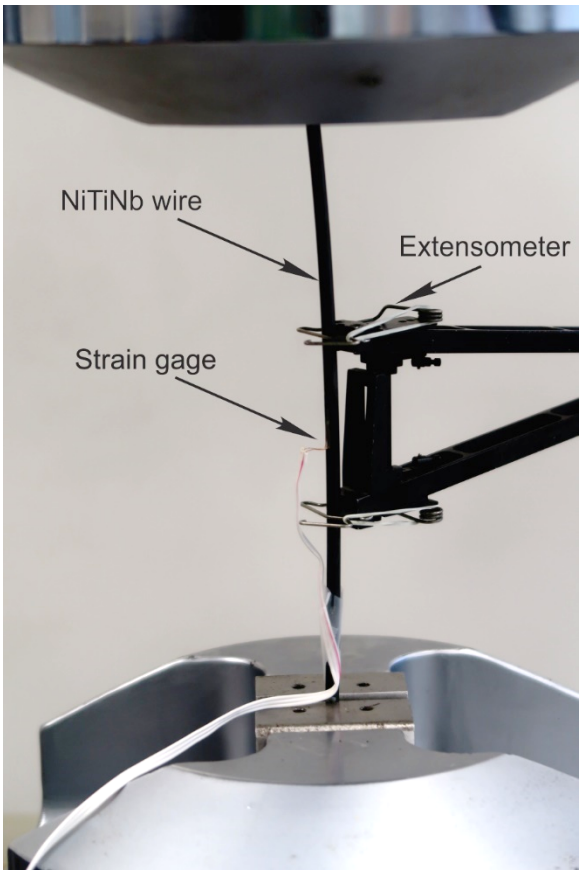

Figure 55. Tensile test setup.

Restrained Recovery Test. The specimens were placed in the testing machine using the hydraulic grips; the sample had a grip length of 2 in. and a total gage length of 7 in. A 2-in. extensometer and Type-K thermocouple were affixed to the specimen (Figure 56a). The test was conducted so that the NiTiNb wire underwent constrained shape recovery (Figure 56). The first phase of the test was conducted by Ohmic heating of the wire by passing approximately 44 A current until the specimen reached at least 170 °C. During shape recovery, recovery load, strain and temperature were recorded. Once the specimen achieved full recovery, the current source was turned off and the specimen was allowed to cool down to room temperature to determine the loss in recovery stress associated with cooling of the wire.

Figure 56. Recovery test setup.

Bond Characterization Test Procedures

Shape-recovery of NiTiNb. With the exception of BOB-AU-N group, all tests on bond characterization test specimens were started by shape-recovery of NiTiNb wire to induce post-tensioning to the specimens. To induce shape recovery in NiTiNb, the exposed ends of the wire were hooked up to a power source. The temperature development was measured with three Type K thermocouples: two of them placed within the debonded region of NiTiNb (Figure 57), and one placed on one exposed end of the wire. During heating, the crack opening displacement (COD) at the notch was measured with a COD clip gage affixed to the specimen with knife edges (Figure 57).

Bond Characterization Tests. Following shape-recovery of NiTiNb, three-point bending tests were conducted (Figure 57) to assess the quality of bond between NiTiNb wire and grout. The tests were performed in a 22-kip MTS universal testing machine in closed-loop control under a COD rate of 0.001 mm/min as the loading rate.

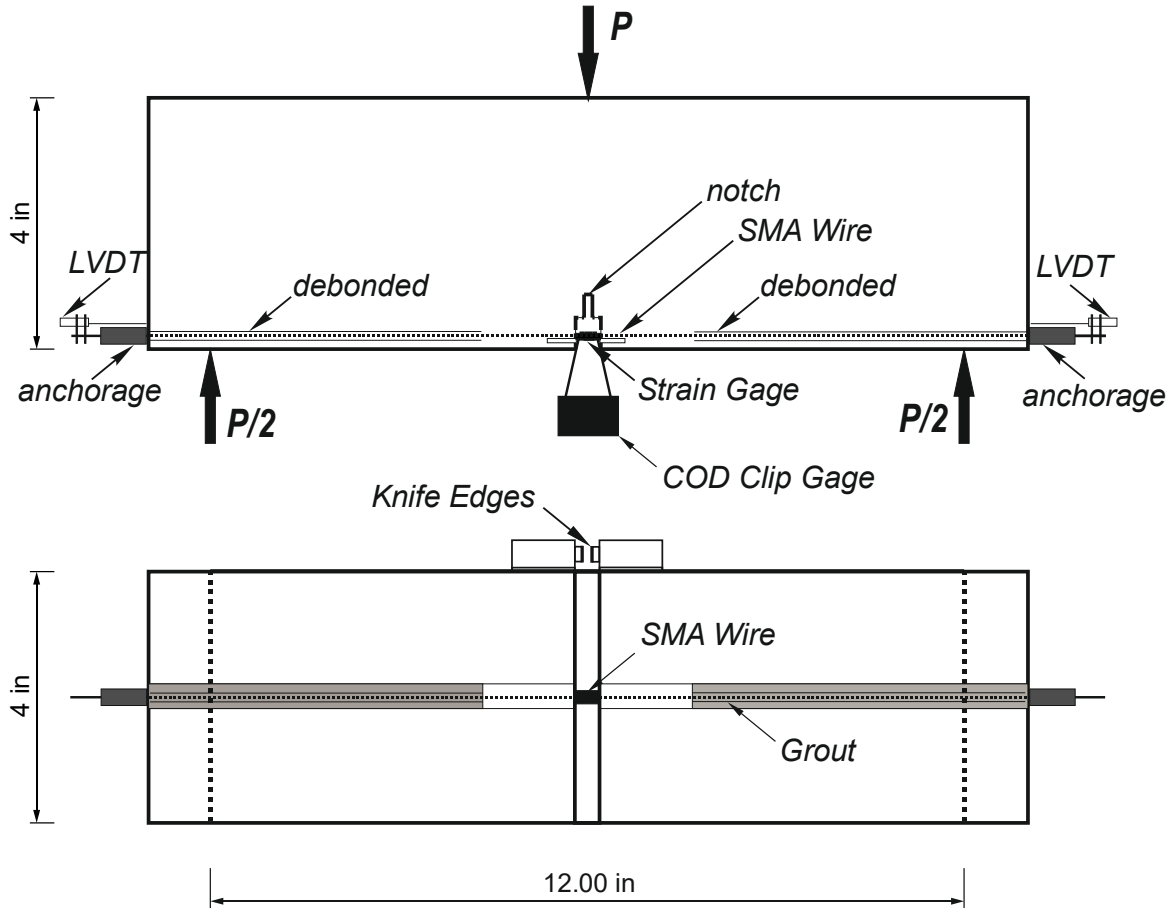

Figure 57. Instrumentation on bond characterization specimens.

Reinforced Concrete Girders Test Procedures

Control reinforced concrete girder (without grooves and NiTiNb wires) was loaded, in stages, up to failure in a four-point flexural setup as shown in Figure 58. Three (3) reinforced concrete girders were cracked to simulate typical girder damage, and tested in the following sequence: (1) post-tensioning the cracked girders by heating the NiTiNb wires to induce shape-recovery; and (2) loading the post-tensioned girders up to failure.

Figure 58. Four-point bending test setup.

Cracking of the Reinforced Concrete Girders. Three (3) reinforced concrete girders, which were to be post-tensioned, were loaded in stages until they developed significant cracks and residual midspan deflection. The girders were supported on 3/4th in. thick neoprene pads and the load was applied with a hydraulic system consisting of Enerpac pump and 100-kip actuator (Figure 59). The pump and the actuator were connected using hoses carrying hydraulic fluid. The load on the girder was distributed using a steel spreader beam (W 8 x 25) to achieve a four-point loading condition (Figure 58). NiTiNb wires were placed in the grooves before cracking and left unanchored to prevent the development of additional strain while loading the girders.

The instrumentation was set up to collect the load, midspan deflection, support deflections and strain in the top fiber of concrete via a LabView based data acquisition system configured with National Instrument modules (Figure 60). The actual midspan deflection was measured by deducting the support deflection from the measured midspan deflection. Once the cracking moment of the girders was exceeded, the cracks were traced and the corresponding loads were marked on the girders with color pens. The final crack widths after cracking the girders were measured with a concrete crack ruler.

(a) (b)

Figure 59. Loading mechanism for the flexural test consisting of: (a) Enerpac pump; and (b) actuator.

Post-tensioning of Reinforced Concrete Girders. The NiTiNb wires were installed at the bottom cover of each of the three cracked girders and kept unbonded throughout the length of the girders. The number of NiTiNb wires in each of the girders was kept as a test variable. Three of the widest cracks were instrumented with LVDTs to monitor the change in crack widths during post-tensioning (Figure 60a). The strain at the top fiber of concrete on either side of the girders were instrumented with strain gages and will henceforth be referred to as SG1 to denote the strain on side 1 (to the negative z-axis) and SG2 to denote the strain on side 2 (to the positive z-axis) as shown in section A-A (Figure 60b). Similarly, LVDTs recording midspan deflection on either side of the girder will be referred to as MD1 for midspan deflection of side 1 and MD2 for midspan deflection of side 2.The LVDTs recording support deflection will be referred to as SD1 and SD2 for the support in the negative x-direction and positive x-direction respectively. The deflection obtained by deducting the average of SD1 and SD2 from the MD1 and MD2 will henceforth be denoted as the effective midspan deflection of side 1 (EMD1) and effective midspan deflection of side 2 (EMD2). The NiTiNb wires were instrumented with K- type thermocouple probes to measure the change in temperature of the wires. The thermocouples were denoted as T1, T2, T3 etc., where the number indicates the wire number on which they were attached. The wires were numbered starting from the side 1 of the first row and proceeding in a clockwise direction up to side 1 of the second row (Figure 61b). The NiTiNb wires were anchored at the ends of the girder using the same strand chucks which were used during the bond characterization tests. The strand chucks were made flush against the steel end plates to minimize prestressing losses as NiTiNb wires underwent shape recovery.

The NiTiNb wires were activated via Ohmic heating by using a power source with a rating of 100 V and 30 A (or 3000 W). At first, 4 wires in the first row (wires numbered 1-4) were heated together (Figure 61) until the temperature of each wire exceeded 150 ºC and subsequently allowed to cool down to ambient temperature. It was ensured that not more than four (4) wires were heated together at any point of time to avoid overloading the power source. The wires in the second row (wires numbered 5-8) were heated individually after providing electrical insulation by wrapping all surfaces of the strand chucks with a heat-resistant scotch tape to prevent contact with the steel end plate (Figure 61b). The crack widths after post-tensioning were also measured and recorded manually using a concrete crack ruler.

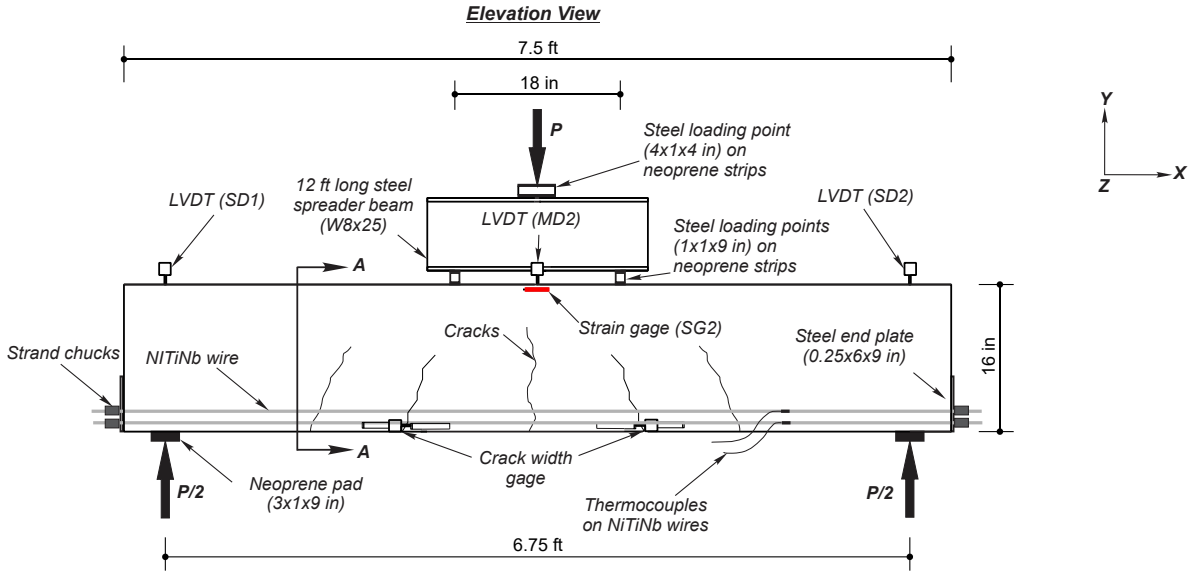

(a)

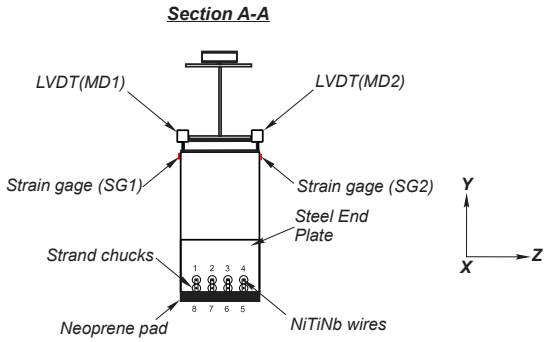

(b)

Figure 60. Instrumentation of reinforced concrete girders: (a) elevation view; and (b) cross-section view.

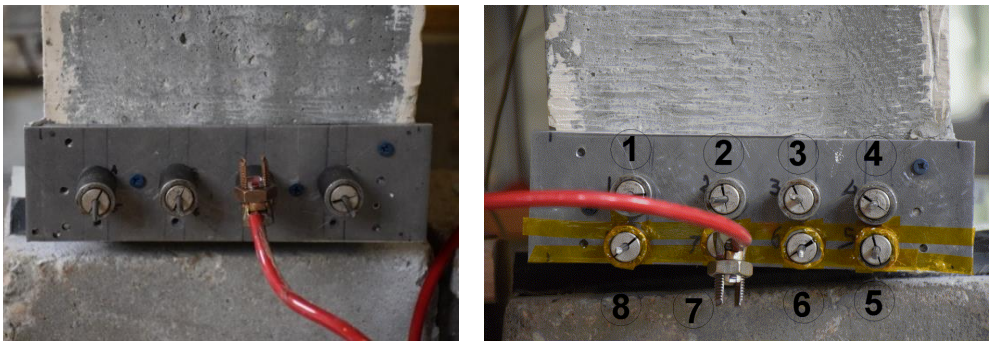

(a) (b)

Figure 61. Heating procedure: (a) wires numbered 1-4; and (b) wires numbered 5-8 in 8-SMA girder.

Flexural Test on Post-tensioned Reinforced Concrete Girders. Four-point flexural tests were performed on the post-tensioned girders by loading them up to failure in four-point bending (Figure 60a, Figure 62). The flexural tests were conducted to observe the change in yield and ultimate moment capacity, cracked stiffness and ductility of the girders after post-tensioning. The loading was carried out in stages: (1) the girder was first loaded beyond cracking moment and unloaded; (2) loaded beyond the yield moment and unloaded; and (3) loaded until the concrete crushed in compression. After every stage of loading, the cracks were traced and the corresponding loads were marked on the girders with a marker pen. The load, midspan deflection, support deflections, strain at the top fiber of concrete and crack width data were recorded. The crack widths were manually measured using a concrete crack ruler after the failure of the girders.

Figure 62. Four-point flexural test after post-tensioning.

DISCUSSION OF RESULTS

Tensile Test Results

Tensile Tests on Austenite

Figure 63 show a typical stress-strain response of NiTiNb samples in austenite phase. The NiTiNb exhibits linear response characterized by an initial modulus of elasticity of approximately 10,000 ksi until the material undergoes transformation to detwinned martensite. The transformation initiates at approximately 85 ksi and is completed at approximately 90 ksi. As expected, detwinned martensite phase demonstrates lower modulus of elasticity than austenite. The test ended by detwinned martensite rupture at approximately 145-150 ksi. The average strain at rupture was found to be 33.5%. Excellent repeatability in test results was observed between the 3 replicates.

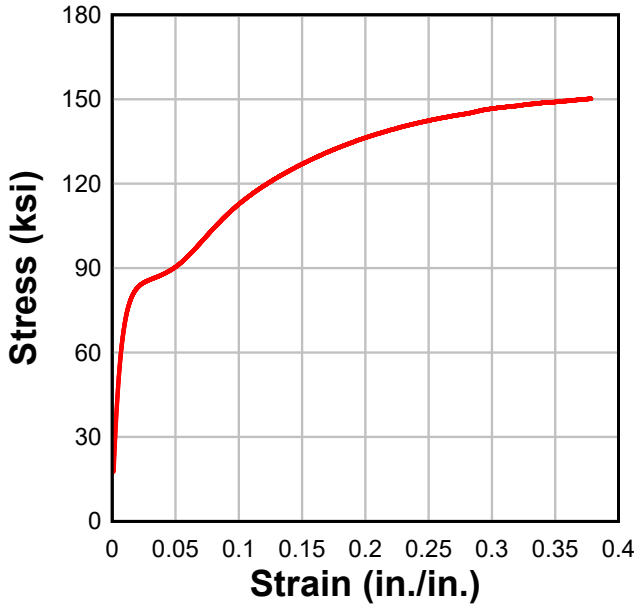

Figure 63. Typical stress-strain curve of NiTiNb in austenite phase.

Restrained Recovery Test

Typical restrained recovery tests results are shown in Figure 64. At the temperature is increased, the recovery stress is generated in the restrained NiTiNb wire. The maximum recovery stress, corresponding to the maximum heating temperature, was approximately 73 ksi. The data also shows that no further recovery stress is generated beyond 150 °C. Once each wire reached at least 180 °C, the power source was turned off and wires were allowed to cool down to ambient temperature (23-25 °C) to determine the residual recovery stress. At

room temperature, each wire retained approximately 92% of the maximum recovery stress (or 67 ksi). Excellent repeatability in test results was observed between the 3 replicates.

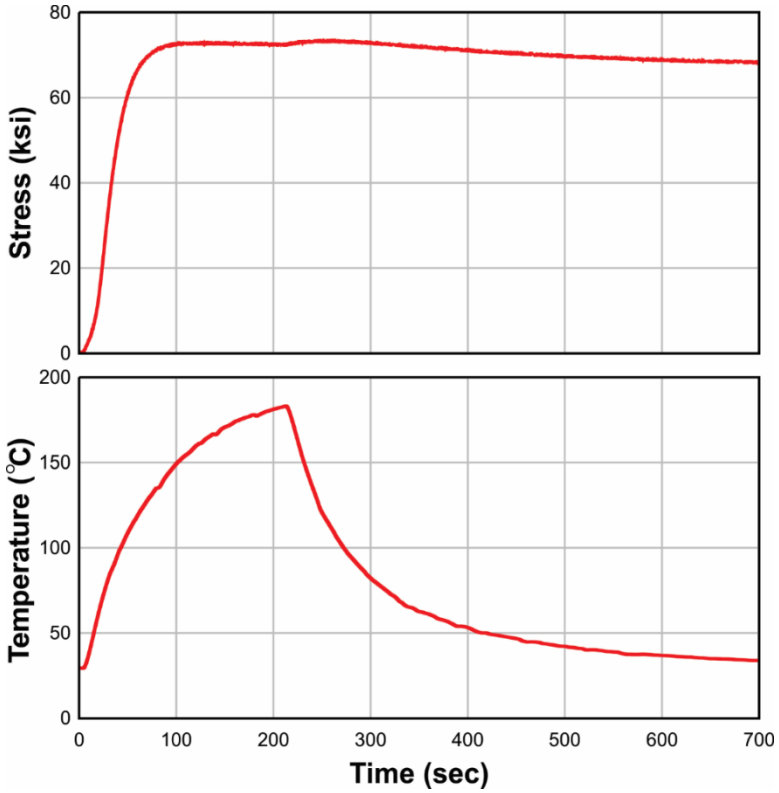

Figure 64. Restrained recovery test results showing relationship between material temperature and generated recovery stress.

Bond Characterization Test Results

Shape-Recovery of NiTiNb

In the bond characterization tests where shape recovery-initiated post-tensioning was performed, temperature was monitored with three thermocouples: two of them placed on the portion of the NiTiNb wire embedded in grout, and one on the exposed portion of the wire. Temperature measurements during shape recovery (Figure 65) clearly indicate that portion of NiTiNb wire in contact with grout is heating at a lower rate than exposed portion of the wire. This is not surprising as the conductivity of concrete is on the order of magnitude of 1.0 W/mK, while that of air is 0.026 W/mK. Heat loss in NiTiNb caused by its contact with grout meant that to reach a temperature approaching that required for complete shape recovery, the heating time had to be significantly increased over that reported in Figure 64; in each specimen the heating was stopped once the exposed portion of the NiTiNb wire reached 250 °C for safety reasons. It was observed that concrete surface temperature was significantly raised once the exposed portion of the wire started to reach 250 °C.

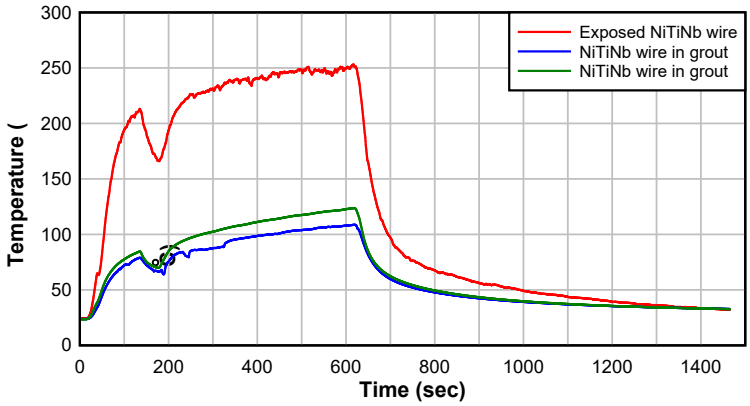

Figure 65. Measured temperatures at different locations on the NiTiNb wire.

The COD measurements during shape recovery (Figure 66) demonstrated reduction in COD as the temperature initially approached the maximum. The COD reduction was more significant in the specimens with anchored NiTiNb wires, which indicates that the bond between the NiTiNb wire and the grout is poor, and that anchorage plays an essential role in the transfer of post-tensioning force. However, even though the temperature was held somewhat constant upon reaching its maximum, the COD in all samples started to increase: this behavior is accredited to the development of a thermal gradient between the top and bottom surfaces of the specimen induced by heating of the wires. Such thermal gradient caused deflection of the specimen downwards which ultimately counteracted the compressive stress at the bottom of the specimen developed via post-tensioning. While the thermal gradient resulted in a change of the stress state at the notch tip from compression to tension in the samples without anchorage, the same did not occur in the specimens with anchored NiTiNb wires. It is expected that the thermal gradient-related crack opening would dissipate as the concrete at the bottom of the specimen cools down. However, the data collection was stopped as soon as the NiTiNb wire temperature approached ambient temperature, so the current data does not provide evidence as to how COD would be affected upon concrete reaching its equilibrium temperature.

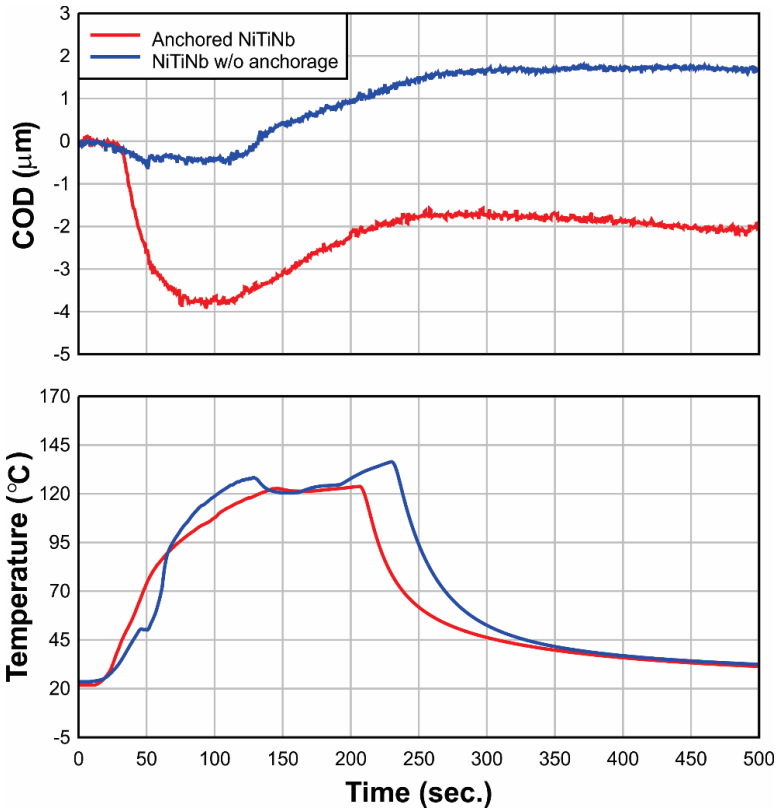

Figure 66. Typical change in COD with NiTiNb shape recovery.

Bond Characterization Tests

Results from typical three-point bending tests, which characterize the bond between the grout and the NiTiNb wire, are shown in Figure 67. The relationship between applied load and COD remains linear until the crack above the notch forms and the load drops. The failure of the specimen is due to the unstable crack growth originating from the notch.

Strength, strain and slip data for all specimens is summarized in Table 8. Specimens without anchorage did not experience notable improvement in strength over control specimens. Interestingly, the specimens reinforced with austenite demonstrated slightly higher strength than that where specimens were post-tensioned with NiTiNb. Post-tensioning of NiTiNb may have introduced stresses that exceed the strength of the bond which would explain why BOB-PT-N group showed no increase in strength over control. Strain measurements in NiTiNb at maximum load (Table 8) indicate very small strains at specimen failure; this is not surprising as given the rigidity of the test setup and relatively small depth of NiTiNb in the cross-section. While no significant slip (Table 8) was observed during loading from 0 to maximum load, LVDTs clearly captured slip between maximum and “residual” load levels indicating bond failure immediately after the specimen strength was reached. It is not clear why there is an order of magnitude higher slip in BOB-AU-N when compared to BOB-PT-N.

It is apparent that presence of anchorage results in an increase of specimen strength over control group: this is thought to be due to the post-tensioning that introduces compressive stress field at the notch at the beginning of the test. The group of anchored specimens where NiTiNb was bonded with grout prior to post-tensioning did not experience as great of an increase in strength as the rest of the anchored group. A possible reason for this behavior is that post-tensioning force is distributed along the bonded region, so the effect of the post-tensioning on the stress state at the notch tip is not as drastic as it is in the unbonded anchored specimens. Strains in NiTiNb at maximum load (Table 8) were small. However, an order of magnitude difference in strain measurements between bonded (BOB-PT-A and BOA-PT-A) and unbonded specimens (UB-PT-A) was observed: this is not surprising as strain is uniformly distributed along the unbonded portion of the NiTiNb, while in bonded specimens localized maximum strain would develop below the notch at the measurement location (Figure 57). LVDT slip measurements (Table 8) in anchored specimens indicated no slip during the test most probably because most of the slip occurred during the transfer of post-tensioning.

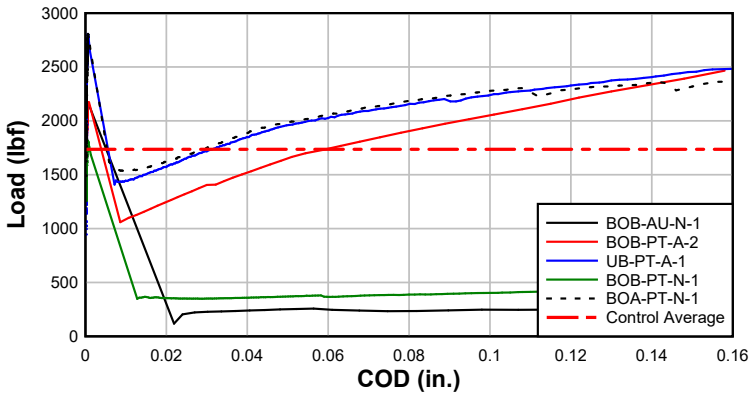

Figure 67. Typical load vs. COD behavior in bond characterization specimens.

Table 8. Summary of flexural specimen strengths.

Specimen	Maximum Load (lbf)	Strain at max. load (με)	Slip between 0 and max. load (in.)	Slip following load drop from max. to "residual" (in)
Control-1	1583.51	n/a	n/a	n/a
Control-2	1889.13			
BOB-AU-N-1	2185.22	374	0	0.036
BOB-AU-N-2	1860.87	68	0	0.089
BOB-PT-N-1	1657.28	-	-	-
BOB-PT-N-2	1823.4	220	0	0.006
BOB-PT-N-3	1797.45	-	0	0.003
BOB-PT-A-1	1936.56	470	- no lvdt used	- no lvdt used
BOB-PT-A-2	2188.82	150		
UB-PT-A-1	2806.51	59	0	0
UB-PT-A-2	2315.67	61	0	0
BOA-PT-A-1	2828.13	693	0	0

Presence of anchorage has a clear influence on the post-cracking behavior of the bond characterization specimens (Figure 67). The specimens without anchorage experienced a sharp drop in load followed by a constant load level due to the friction between the NiTiNb wire and grout. On the contrary, in the specimens with anchorage, the load picks up quickly after the initial crack formation until the test is interrupted upon COD gage reaching its maximum opening displacement of approximately 0.16 in. The increase in load is possible because anchorage allows NiTiNb wire to carry tensile force which provides additional moment capacity to the specimen.

Once the specimens without anchorage were unloaded there was no significant change in the final crack width. Anchored specimens, however, exhibited an interesting behavior induced by superelastic recovery of NiTiNb (Figure 68). Following unloading, COD returned to zero and a crack in the top of the specimen formed due to the tensile stress generated by

superelastic recovery of NiTiNb. Once again, the observed behavior demonstrates the advantage of using anchorage in conjunction with NSM NiTiNb reinforcement.

Evaluation of strain developed in NiTiNb wire in an anchored specimen (Figure 69) shows a significant increase in strain following initial cracking, proving that following cracking NiTiNb begins to provide the tensile capacity to the specimen. Upon unloading the strain recovers due to a superelastic effect and goes into compression which ultimately leads to the development of tensile stress at the top of the specimen and subsequent cracking (Figure 68 photograph no. 4).

The effectiveness of strand chucks as anchorage was also confirmed via post-mortem inspection of the anchored portion of NiTiNb wires. Micrographs of the wire surface clearly show a well-developed pattern of bite marks (Figure 70) indicating that jaw segments were effective at preventing lateral sliding of the wire.

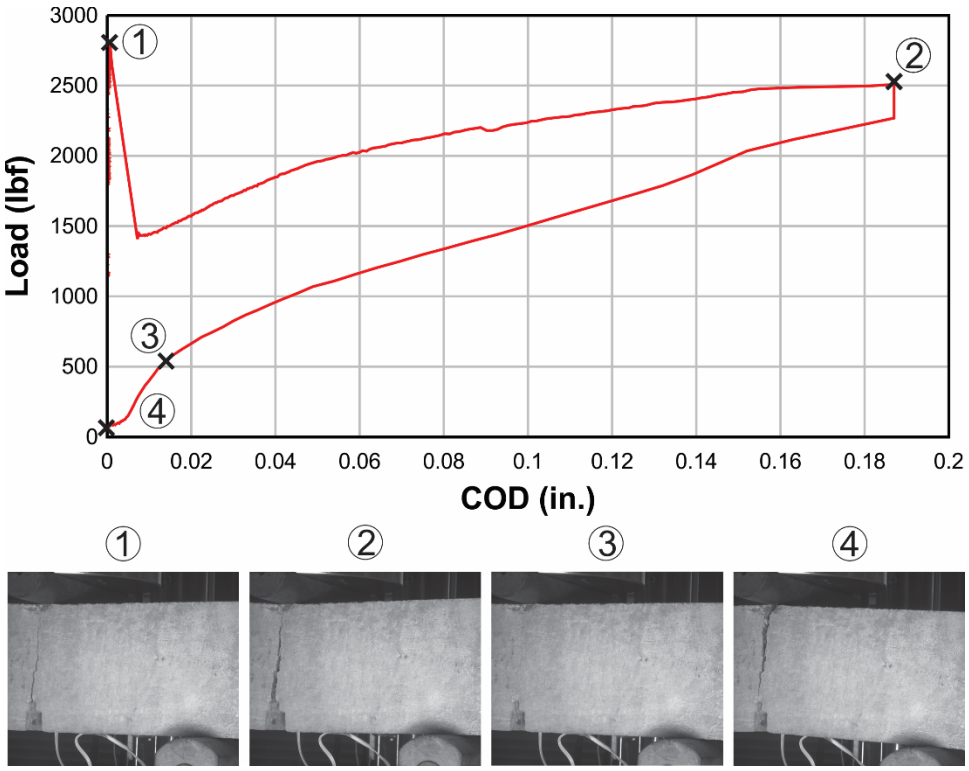

Figure 68. Typical load vs. COD behavior of anchored specimens (plotted here is specimen UB-PT-A-1): (1) initial crack formation; (2) maximum crack opening; (3) crack closure induced by superelastic recovery of NiTiNb; (4) crack formation at the top of the specimen induced by superelastic recovery of NiTiNb.

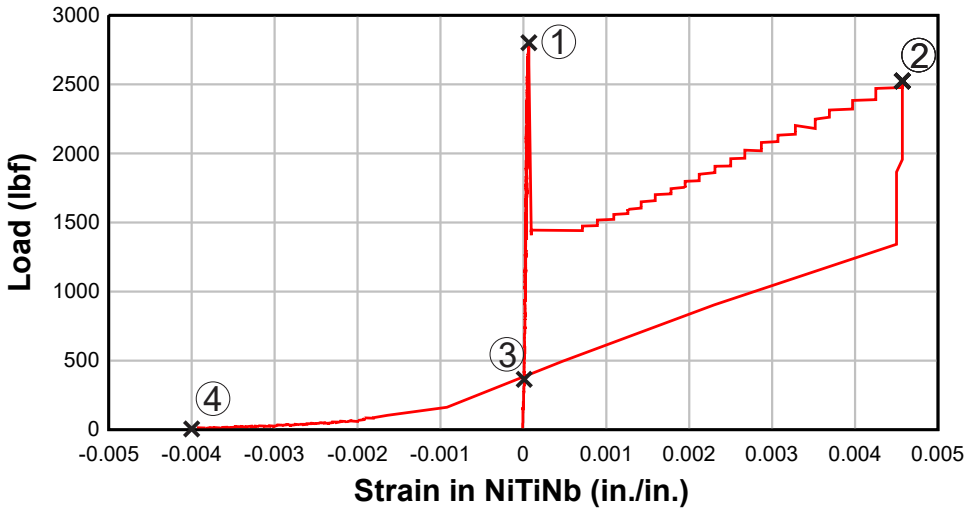

Figure 69. Typical load vs. strain in NiTiNb plot for anchored specimens (plotted here is specimen UB-PT-A-1); number marks 1-4 relate to photographs in Figure 68.

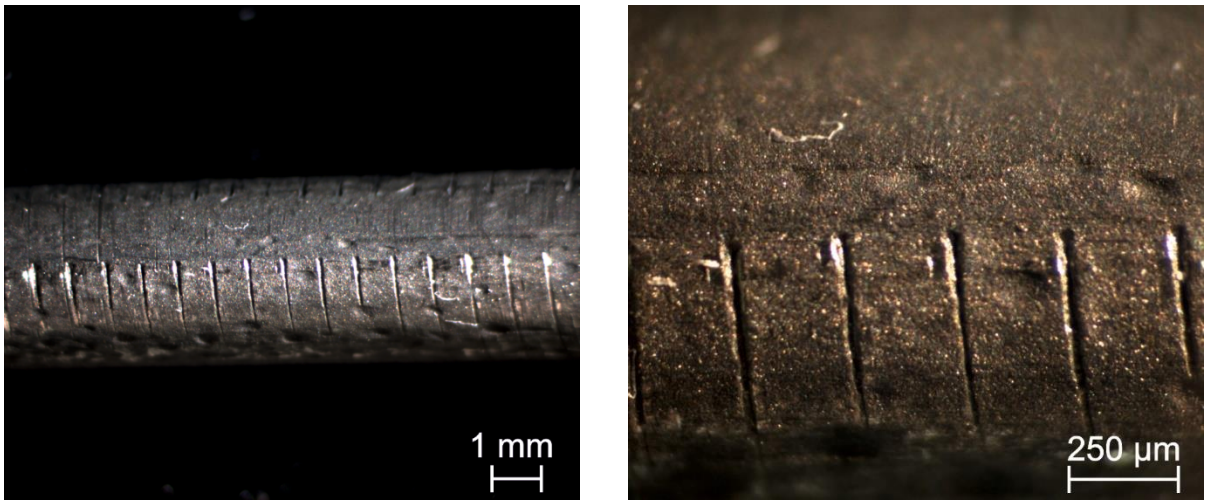

(a) (b)

Figure 70. Bite marks on anchored portion of NiTiNb wire.

Reinforced Concrete Girder Test Results

Post-Tensioning of Cracked Reinforced Concrete Girders

Prior to post-tensioning, three (3) reinforced concrete girders were cracked by loading them in stages. The extent of cracking the girders significantly influenced their behavior during post-tensioning. A Control girder without grooves or NiTiNb wires was loaded up to failure before cracking the girders to be post-tensioned. The yield moment of the Control girder was found to be 45 kip-ft and the girders to be post-tensioned were cracked up to a moment which is expressed as a multiple of the yield moment of Control girder. The 8-SMA, 10-SMA and 12-SMA girders were cracked up to 0.89, 1.15 and 1.06 times the yield moment of

the Control girder, respectively. A summary of the crack width, stiffness of cracked girders and residual midspan deflection is provided in Table 9.

Table 9. Summary of the results after cracking the girders to be post-tensioned.

Specimen	Maximum crack width (mm)	Cracked Stiffness (kip-ft/in.)	Residual Midspan Deflection (in.)
8-SMA	0.18	305.5	0.075
10-SMA	0.64	299.4	0.175
12-SMA	0.64	269.6	0.115

The effectiveness of post-tensioning tests on the cracked girders was evaluated by observing the variation of crack widths, residual midspan deflection and tensile strain at the top fiber of concrete with temperature as shown in Figure 71 (8-SMA), Figure 72 (10-SMA) and Figure 73 (12-SMA). Since the girders were instrumented on each side (of the cross-section) to measure the residual midspan deflection and strain on the top fiber of concrete, it is essential to define the sides of the girders as side 1 and side 2 (as discussed according to Figure 60a and Figure 60b) before the results are discussed. The residual midspan deflection is referred to as EMD1 and EMD2, and the strain is referred to as SG1 and SG2 (as explained with reference to Figure 60b) to discuss the results of the post-tensioning tests. It should be noted that due to malfunction of the acquisition system, the data during post-tensioning of wires numbered 6 to 10 in the 10-SMA girder were not recorded. The data at the end of the post-tensioning was recorded and the transition from the time when the data stopped recording until the end of post-tensioning is represented by a dotted line (Figure 72).

The crack width was found to decrease as the NiTiNb wires were heated above 150 ºC. The decrease in crack widths was due to the compressive post-tensioning force transferred from the NiTiNb wires to the concrete via end anchorage. The crack widths reduced as the number of NiTiNb wires in the girders increased; the maximum reduction of crack width (74%) was observed in the 12-SMA girder. The crack width stopped reducing midway through the post-tensioning process in the 8-SMA girder. A possible reason for this behavior is that the crack widths in the 8-SMA girder were relatively narrower than the 10-SMA and 12-SMA girders after cracking (as seen from Table 9).

As per ACI 224R-01 [31], the acceptable limit of crack widths is 0.41 mm for structures in dry air or protected by membranes, and 0.30 mm for structures in humid and moist air or surrounded by soil. From the post-tensioning results, it was observed that the crack widths were reduced well below 0.30 mm for the girders in laboratory condition. Hence, it can be concluded that the crack widths of the post-tensioned girders are well within the acceptable limits for the conditions mentioned above. The crack widths for structures subject to deicing chemicals and exposed to seawater environments have lower acceptable limits (0.18 and 0.15 mm, respectively) and the crack widths observed in the post-tensioned girders do not fall under those limits. Nonetheless, the results clearly indicate that the proposed post-tensioning method significantly reduces the crack widths.

The residual midspan deflection also decreased with the increase in temperature in the NiTiNb wires throughout post-tensioning. The negative moment introduced by the compressive post-tensioning force in the NiTiNb wires was responsible for the reduction in residual midspan deflection. The EMD1 and EMD2 for all the post-tensioned girders are in good agreement (Figure 71, Figure 72 and Figure 73). The 8-SMA showed a lower reduction in residual midspan deflection (0.065 in. to 0.036 in.) due to lower post cracking stiffness and residual deflection after cracking, relative to the 10-SMA and 12-SMA girders. The post-tensioning reduced the residual deflection from 0.17 in. to 0.102 in. in 10-SMA girder and from 0.114 in. to 0.058 in. in the 12-SMA girder. Although the magnitude of reduction is higher in case of 10-SMA girder, it should be noted that the residual deflection after cracking was higher in the 10-SMA girder. Hence, it follows that the reduction of residual deflection was the higher in the 10-SMA girder, even though higher post-tensioning force was generated in the 12-SMA girder.

The post-tensioning forces in the NiTiNb wires led to the development of compressive stress at the bottom of the girders. Subsequently, a tensile stress developed at the top fiber of concrete which led to the tensile strain increasing steadily as the wires were heated (Figure 71) in all the post-tensioned girders. The increase in tensile strain cannot be correlated to the number of NiTiNb wires responsible for post-tensioning due to the discrepancy in SG1 and SG2 in all the girders. For example, the SG2 in the 10-SMA girder ($180x10^{-6}$ in. /in.) is significantly higher than the SG1 ($100x10^{-6}$ in. /in.). This behavior may have resulted from the imperfections in geometry induced by defects in the formwork while casting the girders and difference in the depth at which SG1 and SG2 were attached. Both of the above-mentioned situations can cause different magnitude of tensile strain to record in SG1 and SG2. Another possible reason for the difference in SG1 and SG2 is the asymmetrical position of the NiTiNb wires in the girders due to improper placement which can result in the generation of uneven post-tensioning forces in either side of the girder.

During heating of some of the wires, the tensile strain in the top of concrete was found to reduce on one side of the girder while increasing on the other side. Following the definition of the sides in the earlier discussion, it can be observed that when a wire adjacent to side 1 is heated (e.g., wire numbered 5 in Figure 71), the SG2 decreases due to lateral bending caused by the eccentricity of wire numbered 5 from the center of the cross-section. Similarly, when a wire adjacent to side 2 is heated (e.g., wire numbered 8 in Figure 71), the SG1 decreases. Similar behavior of the SG1 and SG2 is observed in the 10-SMA and 12-SMA girders.

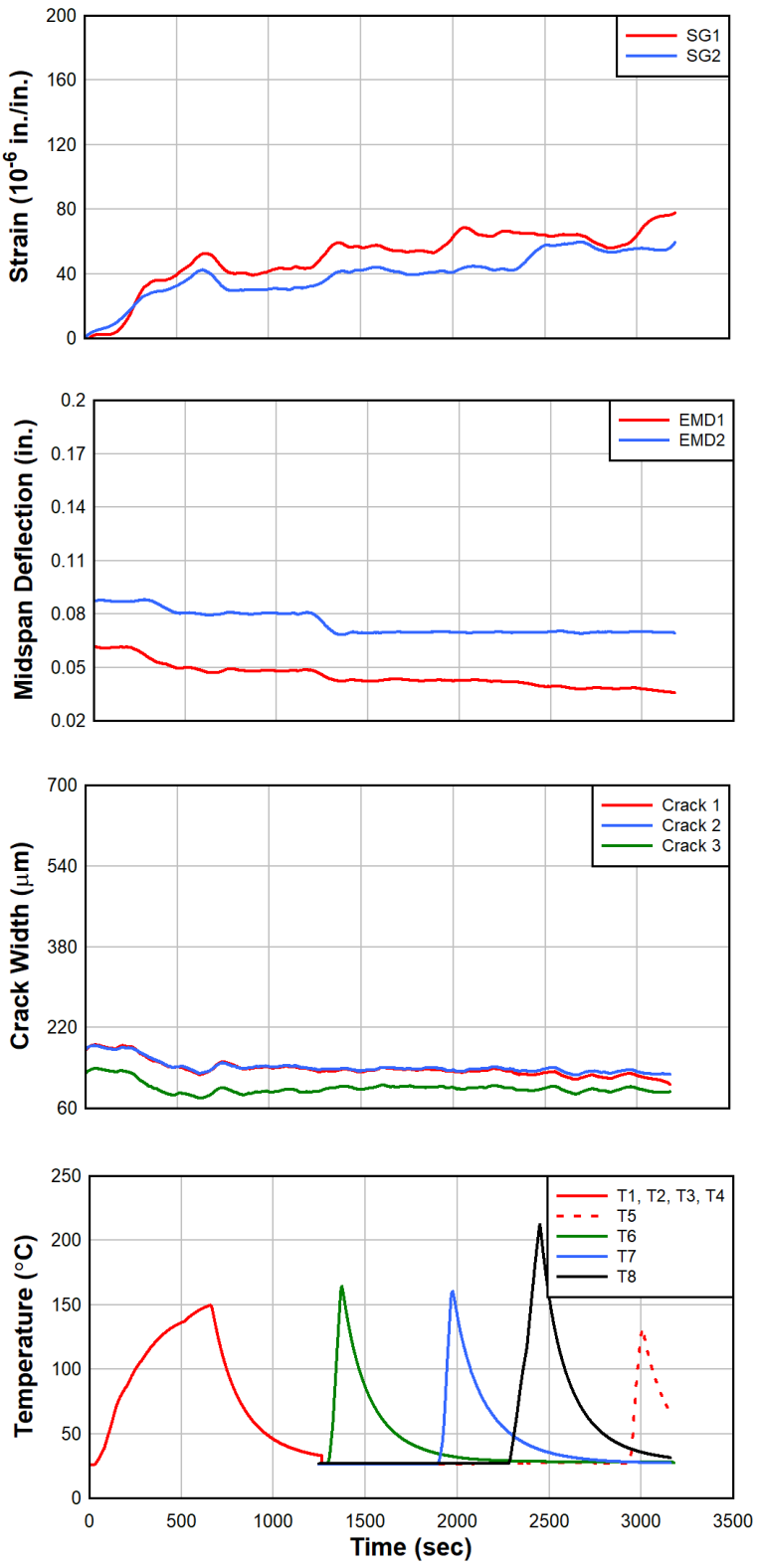

Figure 71. Variation of strain on the top fiber of the middle of girder, residual midspan deflection, and crack width with temperature of 8-SMA girder.

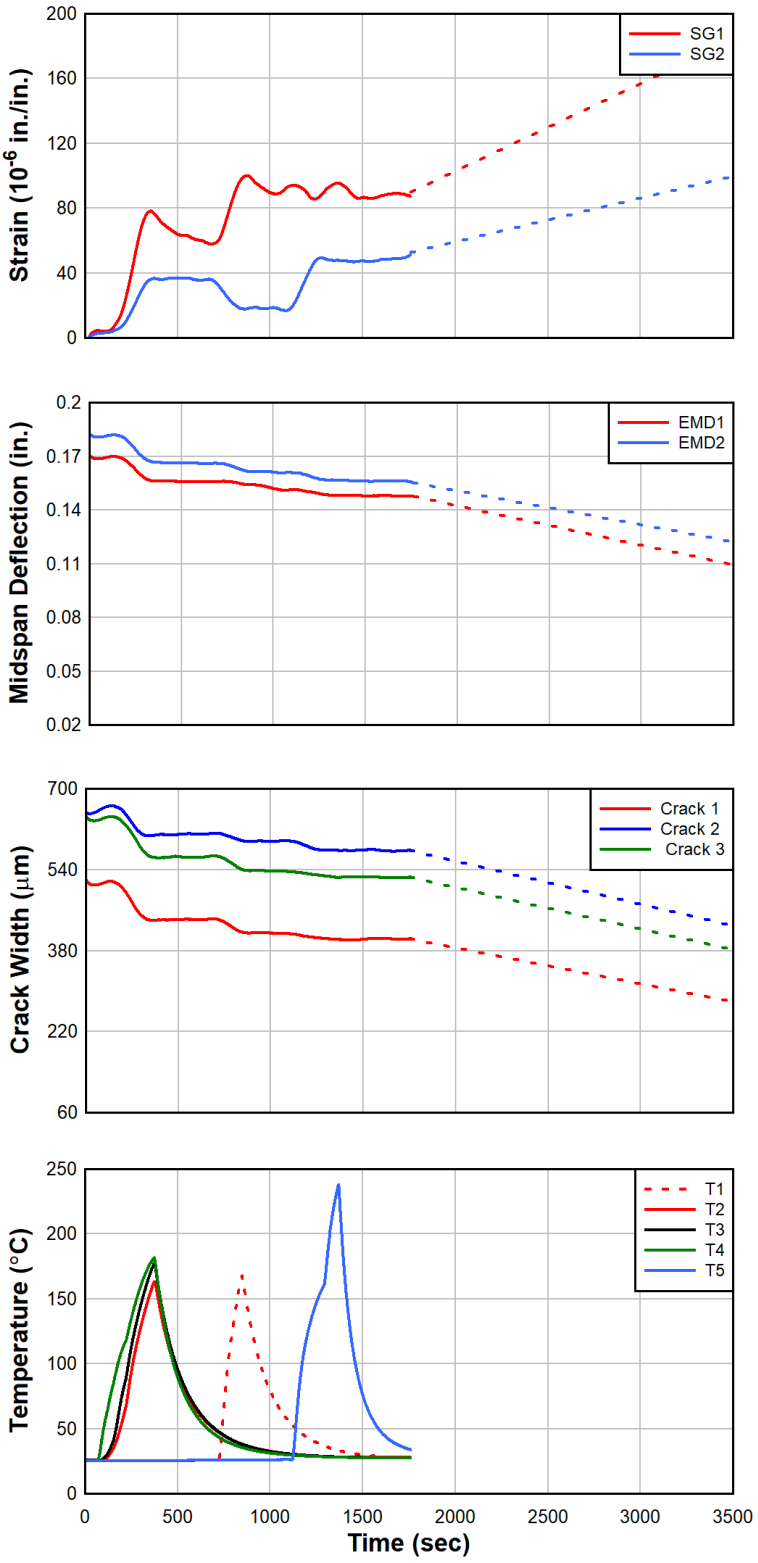

Figure 72. Variation of strain on the top fiber of the middle of girder, residual midspan deflection, and crack width with temperature of 10-SMA girder.

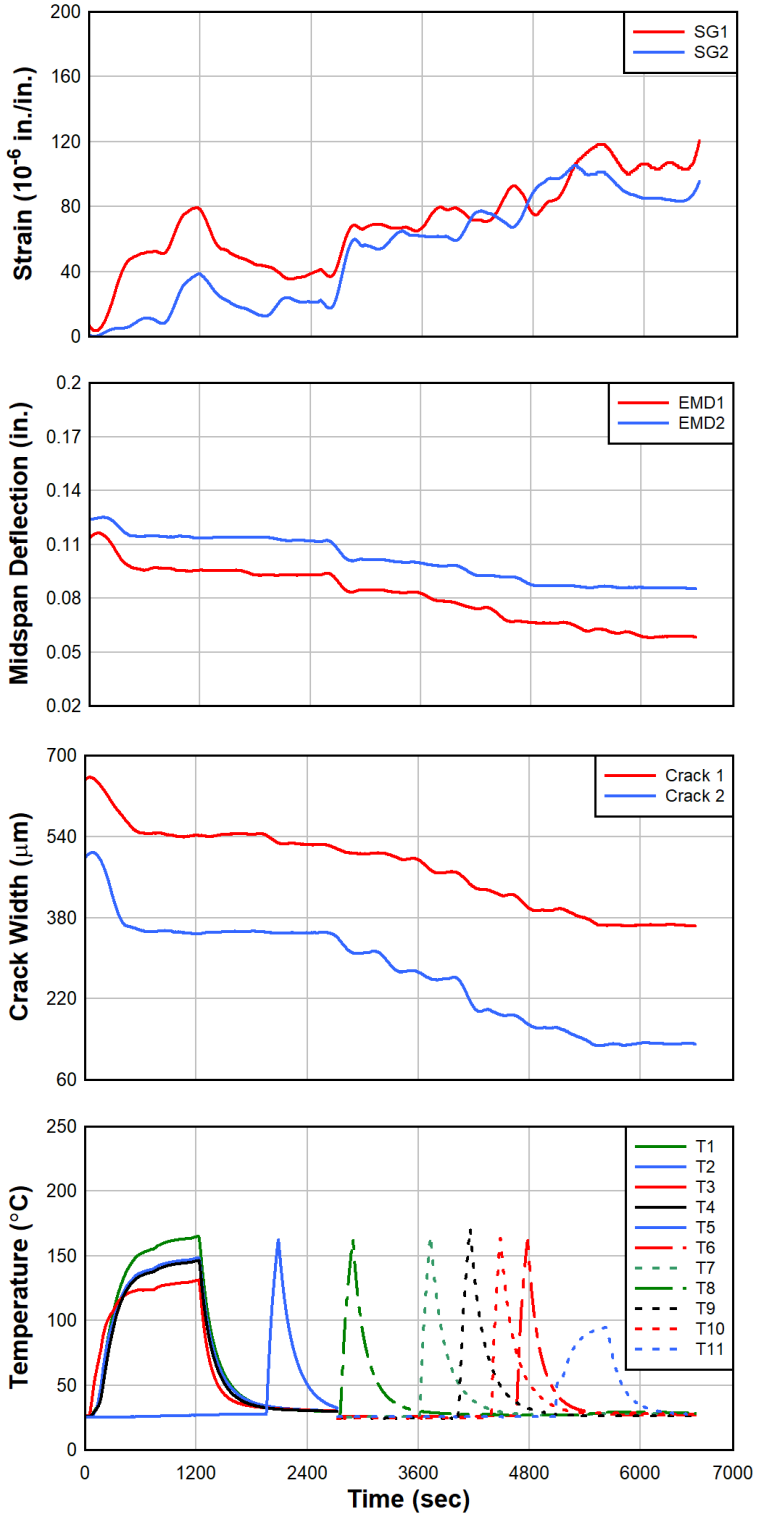

Figure 73. Variation of strain on the top fiber of the middle of girder, residual midspan deflection, and crack width with temperature of 12-SMA girder.

Table 10. Summary of post-tensioning test results.

Specimen	Crack width reduction (%)	Residual midspan deflection recovery (in.)	Tensile strain in top fiber of concrete (10^{-6} in./in)
CONTROL	n/a	n/a	n/a
8-SMA	27-39	0.017-0.026	59-77
10-SMA	34-45	0.058-0.06	100-180
12-SMA	45-74	0.046-0.056	95-121

Flexural Tests on Post-Tensioned Reinforced Concrete Girders

Four-point flexural tests were conducted on the post-tensioned girders by loading the girders in stages up to failure. Control girder was loaded up to failure to serve as a baseline for comparing the behavior of the post-tensioned girders. The yield moment, ultimate moment capacity, cracked stiffness, and deflection ductility coefficient of the post-tensioned girders were compared to those of the Control girder. The cracked stiffness was determined by calculating the slope of the loading portion of the moment vs. deflection curve following initial girder cracking in Control girder, or the slope of moment vs. deflection curve before yield in the post-tensioned girders. The deflection ductility coefficient (μ) is defined by the following equation:

$$\mu = \frac{\Delta_u}{\Delta_y}$$

where Δ_u is the deflection of the girder when the concrete in compression crushes and Δ_y is the deflection at which the girder first yields.

The moment vs. deflection behavior of the Control and post-tensioned reinforced concrete girders are shown in Figure 74. The post-tensioned girders have two parts in the moment vs. deflection curves: (1) the cracking of the girders prior to post-tensioning; and (2) the flexural loading after post-tensioning. The deflection at the start of loading of the post-tensioned girders is less than the deflection after cracking due to the recovery in residual deflection via post-tensioning, as marked in Figure 74. The moment vs. deflection diagrams of the girders clearly indicate a significant increase in yield moment in post-tensioned girders (up to 58%) as compared to the Control girder (Figure 74). The addition of tensile reinforcement in the

form of NiTiNb wires was responsible for the higher yield moment in the post-tensioned girders. The cracked stiffness of the girders was found to increase by up to 31% after post-tensioning due to a higher cracked moment of inertia resulting from the addition of NiTiNb wires.

The ultimate capacity of the post-tensioned girders was significantly higher (up to 45%) than that of the Control girder (Figure 74) due to the tensile stress carried by the NiTiNb wires in addition to the steel reinforcement. The 8-SMA girder had a lower increase in the ultimate moment capacity (35%) than the 10-SMA and 12-SMA girders because of the fewer number of NiTiNb wires. The greatest increase in the ultimate moment capacity was observed in the 10-SMA girder despite the 12-SMA girder having the maximum number of NiTiNb wires. The reason for this anomaly is that cracking and spalling of concrete had occurred near the supports of 12-SMA during loading (Figure 76). Grooves were introduced in the side cover near the bottom of the 12-SMA girder to accommodate the NiTiNb wires and were not grouted after installing the wires. The compressive reaction forces from the supports during loading led to the development of shear stress around the side grooves near the supports causing cracking and spalling of concrete and subsequent bearing failure.

Even though the ultimate deflection capacity in post-tensioned girders did not change significantly from Control (as evidenced in Figure 74 and Table 11), comparison between deflection ductility coefficients of the girders showed that ductility had reduced in the post-tensioned girders. The addition of NiTiNb wires increases the tensile reinforcement of the post-tensioned girders which leads to a higher deflection at mild steel yield. At concrete crushing, the addition of NiTiNb wires reduces the strain in steel reinforcement and increases the depth of the neutral axis which leads to a reduction in section curvature. Hence, the ductility coefficient in the post-tensioned girders is reduced with respect to the Control girder.

The recovery of midspan deflection after each stage of loading in the post-tensioned girders is compared with the Control girder in Figure 75. In this plot, the recovery of deflection is plotted with respect to the ratio of the maximum moment at a loading stage and the ultimate moment capacity (M/M_{ult}). Complete recovery of deflection is observed in all the girders before reaching the yield moment. Beyond yield, the post-tensioned girders show a higher recovery of deflection with an increase in moment than the Control girder. Since the steel was deformed beyond its elastic limit, the recovery of deflection after each loading stage was mainly governed by the number of NiTiNb wires. Due to the highest number of NiTiNb wires, 12-SMA girder shows the highest recovery in deflection after unloading (60%) after unloading the 12-SMA girder after the first yield. The recovery in post-tensioned girders decreases after the subsequent loading stages after yield but remains greater than the Control

girder. The Control girder had only steel as tensile reinforcement and once the steel yielded, large residual deflection was observed after each stage of loading. The presence of post-tensioning forces in the girders prior to loading is a possible reason for greater deflection recovery than Control girder. Greater recovery in post-tensioned girders can also be attributed to the NiTiNb superelastic recovery after the wires were stressed beyond their detwinning stress.

Cracking was observed in all girders during each flexural test and is shown in Figure 77. It was noted that the largest crack width in the Control girder was 5 mm, whereas the largest crack width in the post-tensioned girders was 3.05 mm. The cracks in post-tensioned girders are narrower because of the compressive forces acting on the girders as a result of post-tensioning prior to loading the girders. Superelastic behavior of austenite NiTiNb wires might have also contributed to the narrower cracks in post-tensioned girders. On the other hand, the absence of post-tensioning force prior to loading and significant plastic strain in the steel reinforcement led to the formation of wider cracks in the Control girder. All the girders except the 12-SMA girder showed similar distributed cracking (Figure 77). The less distributed cracking in the 12-SMA girders might be an effect of the greater number of NiTiNb wires as well as the premature failure at the support. Further research is needed to understand and quantify the effect of high SMA reinforcement ratio on the cracking pattern and ductility of the reinforced concrete girders.

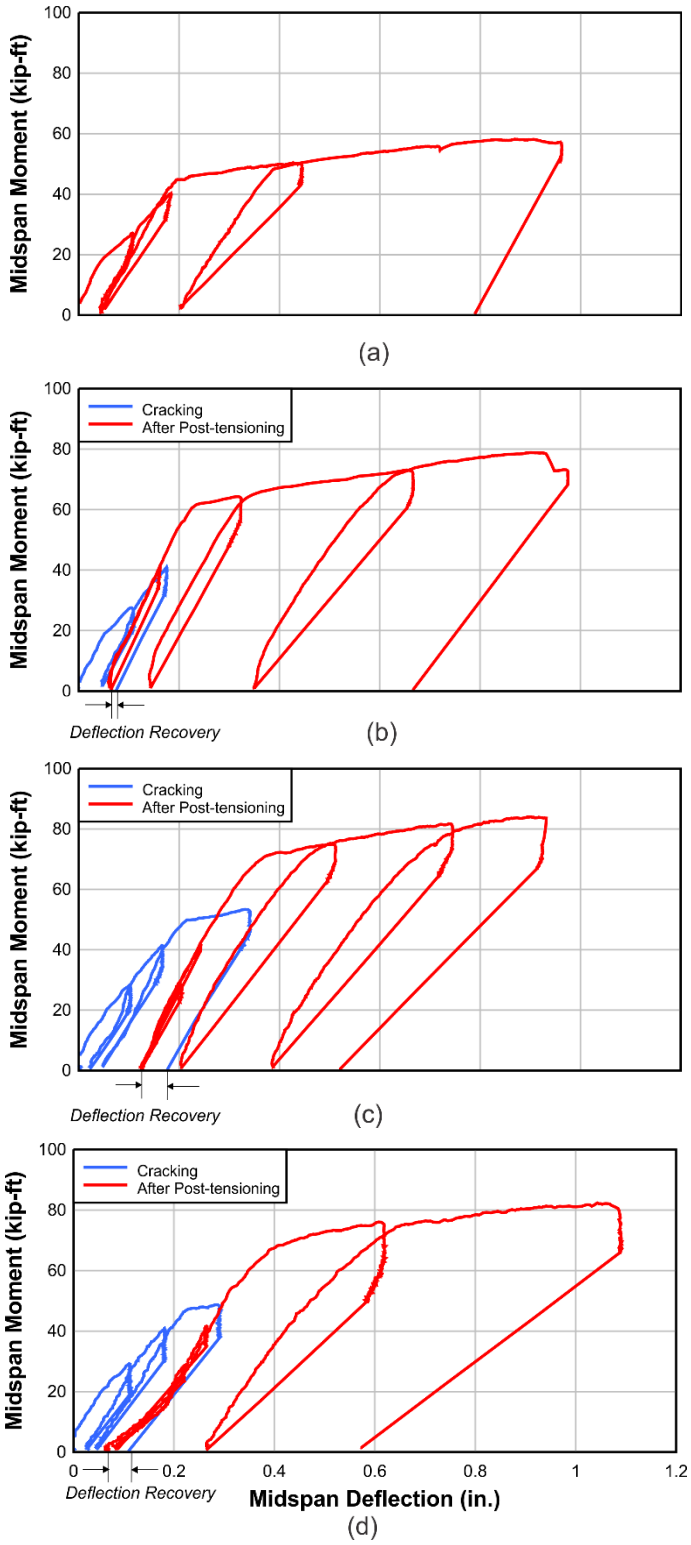

Figure 74. Moment vs. deflection curves of: (a) Control; (b) 8-SMA; (c) 10-SMA; and (d) 12-SMA girders.

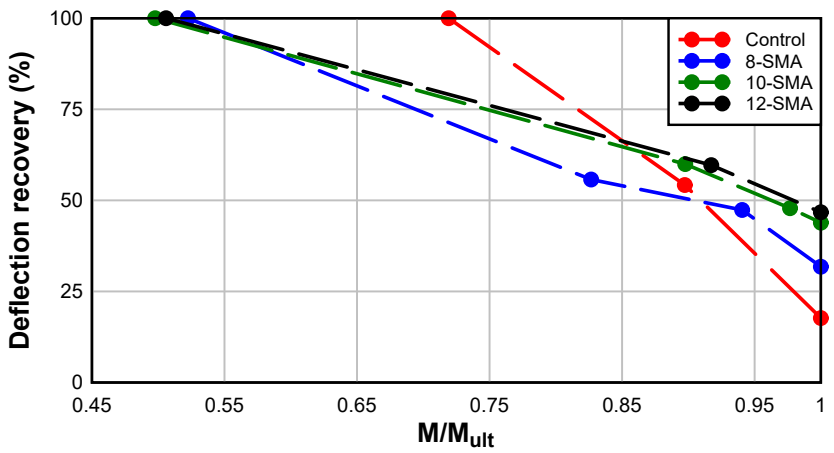

Figure 75. Recovery of midspan deflection after each stage of loading.

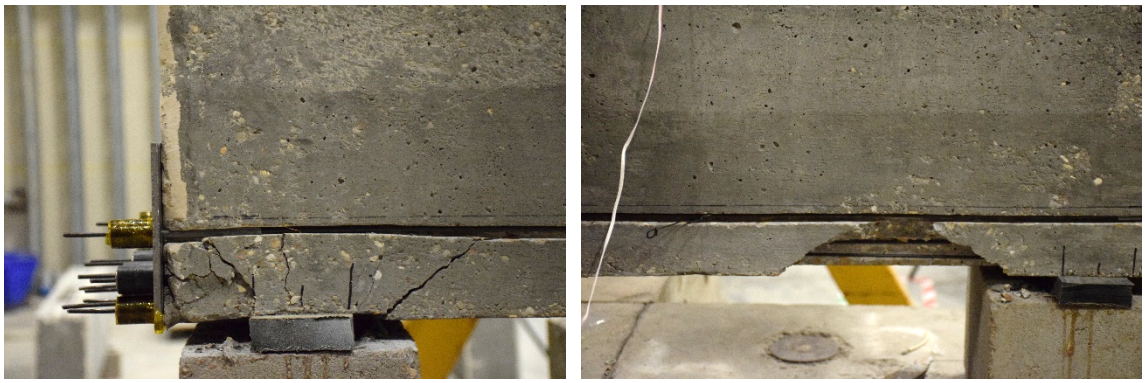

(a) (b)

Figure 76. Girder with grooves in the side cover showing: (a) cracking; and (b) spalling at support regions.

Table 11. Summary of the results of the four-point flexural tests.

Specimen Type	Yield Moment (kip-ft)	Ultimate Moment capacity (kip-ft)	Cracked stiffness (kip-ft/in.)	Ultimate deflection (in.)	Deflection Ductility Coefficient
Control	44.79	57.91	294.67	0.96	4.86
8-SMA	61.67	78.05	327.62 (after post-tensioning)	0.97	4.09
10-SMA	70.83	83.68	346.15 (after post-tensioning)	0.93	2.60
12-SMA	68.02	81.6	337.56 (after post-tensioning)	1.07	2.72

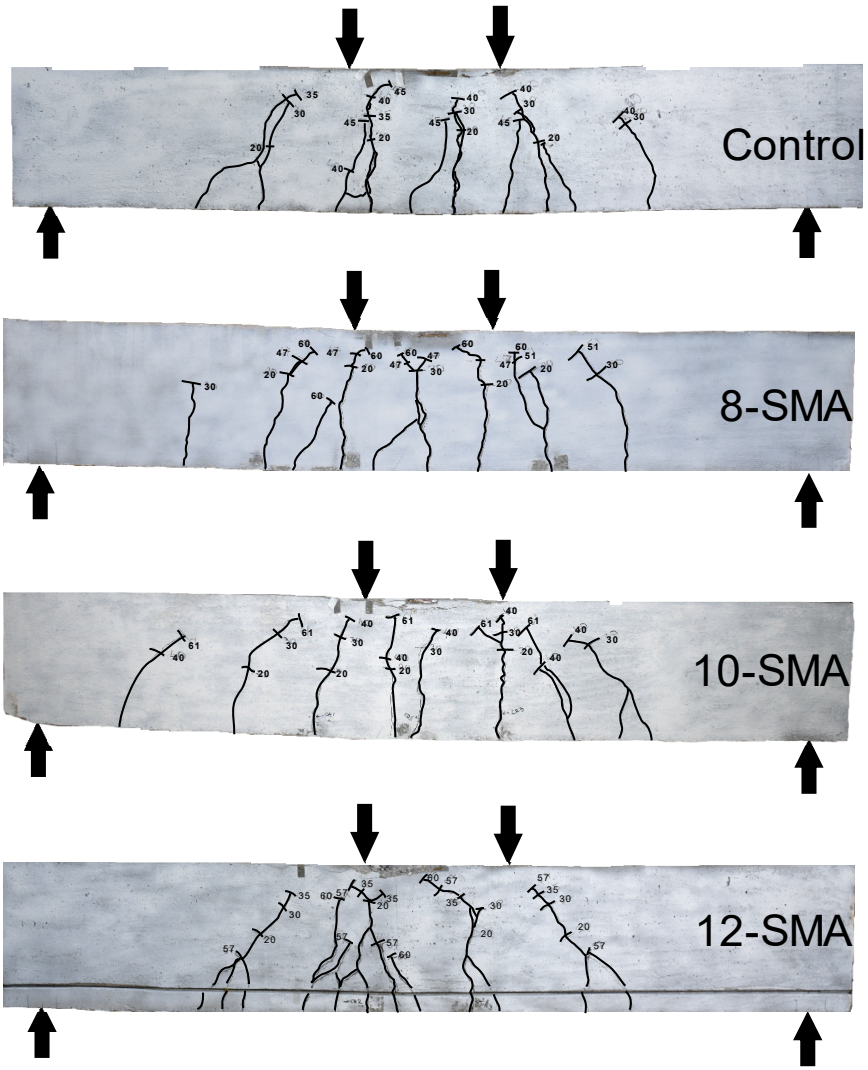

Figure 77. Crack patterns of the reinforced concrete girders after failure. Numbers indicate load in kips.

CONCLUSIONS

The goal of the presented work was to verify the feasibility of using heat-induced post-tensioning in existing cracked reinforced concrete girders through the implementation of shape memory alloys (SMAs) that can recover their original shape upon heating above the material's transformation temperature. In this study, use of near-surface mounted (NSM) NiTiNb alloy wires is proposed for post-tensioning of bridge girders without the conventionally experienced problems with anchorages, high construction costs, long lane closure times, long construction times, etc. A series of experiments were performed to evaluate the proposed strengthening method: (1) tensile tests on austenite to determine the stress-strain behavior of NiTiNb; (2) restrained recovery tests to characterize the post-tensioning potential of NiTiNb; (3) bond characterization tests on notched plain concrete specimens reinforced with NiTiNb wires to test the bond between the NiTiNb wires and cementitious grout; (4) post-tensioning tests on cracked reinforced concrete girders to verify the feasibility of post-tensioning on structural-scale girders; and (5) four-point flexural tests on post-tensioned reinforced concrete girders to observe the changes in yield moment, ultimate moment capacity, cracked stiffness and deflection ductility coefficient following post-tensioning. Below is the summary of the main findings.

- Tensile tests on austenite indicated that the material has initial elastic modulus of 10,000 ksi, with detwinning initiation stress of approximately 85 ksi and ultimate strength of approximately 150 ksi.
- Under restrained recovery test, 2.5%-prestrained NiTiNb wires achieved a maximum recovery stress of 73 ksi at 150 °C. Following cooling to ambient temperature, the wires retained about 92% of the maximum recovery stress, or 67 ksi.
- NiTiNb wires embedded in grout heat up at a much slower rate than those exposed to air. This is due to a relatively large thermal conductivity of grout and concrete.
- Post-tensioning of the notched bond characterization specimens via heat-induced shape-recovery of NiTiNb was most successful in the specimens with anchored wires, as indicated by reduction in COD during heating.
- Bond characterization tests indicated poor bond between NiTiNb and cementitious grout. Significant improvement in bond was accomplished when strand chucks were used as anchorage.
- Bond characterization specimens post-tensioned with NiTiNb wires demonstrated superelastic behavior following unloading which manifested in crack closure in the notched bond characterization specimens.

- Post-tensioning of cracked reinforced concrete girders resulted in a 34-74% reduction in crack widths; the largest reduction was observed in the girder which was post-tensioned with the maximum number of NiTiNb wires (12-SMA).
- The residual midspan deflection was recovered by up to 0.06 in. after the post-tensioning was completed. The post-cracking stiffness and residual midspan deflection after cracking influenced the extent of the recovery of residual midspan deflection.
- Up to 180×10^{-6} in. /in. tensile strain developed on the top fiber of concrete which provided further evidence of the post-tensioning.
- Following post-tensioning the cracked girders, an increase in the yield moment (38-58%) and ultimate moment capacity (35-45%) was observed over the Control girder.
- Grooves introduced in the side covers of girders to accommodate NiTiNb wires should be grouted around the support region to avoid cracking and spalling of the concrete in those areas.
- The cracked stiffness of the post-tensioned girders increased by up to 31% over the cracked stiffness before post-tensioning.
- The post-tensioned girders demonstrated up to 47% decrease in deflection ductility coefficient when compared to the Control girder despite of having similar ultimate deflection capacity.

RECOMMENDATIONS

The proposed post-tensioning technique shows promise for success but the construction methodology for installation of the wires in the damaged girders needs to be refined. The procedure used should be such that it requires easily available machineries and minimizes the repair time. The heating system used should be able to provide sufficient power to heat up all the wires at the same time; activation by open-flame gas torch should be explored.

The presented results suggest that anchorage must be provided to ensure proper transfer of post-tensioning force and improvements in the strength of the repaired/strengthened girders. Authors also recommend heat-induced post-tensioning to be conducted on unbonded NiTiNb wires to avoid difficulties with heat loss to grout and concrete. Since the bond between NiTiNb and grout is poor, subsequent filling of the groove with grout is optional. In fact, it may be beneficial to leave the wires exposed to facilitate future structural health monitoring, inspections, and maintenance.

Fatigue testing of the structures using SMA wires needs to be conducted to observe the behavior of the repaired structures when subject to cyclic loading. Additional work is required to determine the durability properties of NiTiNb when exposed to the aggressive environments which are typically experienced by bridges in northern regions and in close proximity to coastal areas. This includes studying the behavior of the wires when exposed to humid and corrosive environment for extended periods of time under sustained loading.

Feasibility of using the SMA in places which experience earthquake shaking should also be studied. This would delve into another attractive property of the NiTiNb which is known as superelasticity. This property can be used effectively in dampers for structures which are subject to excessive displacements under earthquakes.

SMA also has the potential of being applied in structural health monitoring where the change in resistance of the NiTiNb wires with strain may be used as a sensor. Combining SMA with other composites may lead to the development of smart structures which would be able to act as a sensor and an actuator at the same time. Hence, this material has a wide spectrum of possible applications which can be researched and developed to be used in structural engineering.

REFERENCES

[1] El-Hacha, Raafat, Soudki, and Khaled, “Prestressed near-surface mounted fibre reinforced polymer reinforcement for concrete structures — a review,” Canadian Journal of Civil Engineering, vol. 40, no. 11, pp. 1127-1139, 2013.

[2] D. C. Lagoudas, "Shape memory alloys: modeling and engineering applications," Springer Science & Business Media, 2008.

[3] X. M. He, L. J. Rong, D. S. Yan, and Y. Y. Li, “TiNiNb wide hysteresis shape memory alloy with low niobium content,” Materials Science and Engineering: A, vol. 371, no. 1, pp. 193–197, Apr. 2004.

[4] T. Sakuma, M. Hosogi, N. Okabe, U. Iwata, and K. Okita, “Effect of Copper Content on Superelasticity Characteristics in Ti-Ni and Ti-Ni-Cu Alloy Wires,” MATERIALS TRANSACTIONS, vol. 43, no. 5, pp. 828–833, 2002.

[5] K. Otsuka and C. M. Wayman, Shape memory materials. Cambridge university press, 1999.

[6] C. Cissé, W. Zaki, X. Gu, and T. B. Zineb, “A nonlinear 3D model for iron-based shape memory alloys considering different thermomechanical properties for austenite and martensite and coupling between transformation and plasticity,” Mechanics of Materials, vol. 107, pp. 1–21, 2017.

[7] H. E. Karaca, I. Karaman, D. C. Lagoudas, H. J. Maier, and Y. I. Chumlyakov, “Recoverable stress-induced martensitic transformation in a ferromagnetic CoNiAl alloy,” Scripta materialia, vol. 49, no. 9, pp. 831–836, 2003.

[8] D. Grant and V. Hayward, “Variable structure control of shape memory alloy actuators,” IEEE Control Systems, vol. 17, no. 3, pp. 80–88, 1997.

[9] P. Soroushian, K. Ostowari, A. Nossoni, and H. Chowdhury, “Repair and strengthening of concrete structures through application of corrective posttensioning forces with shape memory alloys,” Transportation Research Record: Journal of the Transportation Research Board, no. 1770, pp. 20–26, 2001.

[10] B. Andrawes and R. DesRoches, “Unseating prevention for multiple frame bridges using superelastic devices,” Smart materials and structures, vol. 14, no. 3, p. S60, 2005.

[11] Z. Deng, Q. Li, and H. Sun, “Behavior of concrete beam with embedded shape memory alloy wires,” Engineering structures, vol. 28, no. 12, pp. 1691–1697, 2006.

[12] H. Li, Z. Liu, and J. Ou, “Behavior of a simple concrete beam driven by shape memory alloy wires,” Smart materials and structures, vol. 15, no. 4, p. 1039, 2006.

[13] K. Dommer and B. Andrawes, “Thermomechanical characterization of NiTiNb shape memory alloy for concrete active confinement applications,” Journal of Materials in Civil

Engineering, vol. 24, no. 10, pp. 1274–1282, 2012.

[14] M. Shin and B. Andrawes, “Experimental investigation of actively confined concrete using shape memory alloys,” Engineering Structures, vol. 32, no. 3, pp. 656–664, 2010.

[15] O. E. Ozbulut, S. Daghash, and M. M. Sherif, “Shape memory alloy cables for structural applications,” Journal of Materials in Civil Engineering, vol. 28, no. 4, p. 04015176, 2015.

[16] S. Kotamala, “Prestressing of simply supported concrete beam with nitinol shape memory alloy,” PhD Thesis, University of Toledo, 2004.

[17] O. E. Ozbulut, R. F. Hamilton, M. M. Sherif, and A. Lanba, “Feasibility of self-pre-stressing concrete members using shape memory alloys,” Journal of Intelligent Material Systems and Structures, vol. 26, no. 18, pp. 2500–2514, 2015.

[18] C. Czaderski, M. Shahverdi, R. Brönnimann, C. Leinenbach, and M. Motavalli, “Feasibility of iron-based shape memory alloy strips for prestressed strengthening of concrete structures,” Construction and Building Materials, vol. 56, pp. 94–105, 2014.

[19] M. S. Saiidi, M. Sadrossadat-Zadeh, C. Ayoub, and A. Itani, “Pilot study of behavior of concrete beams reinforced with shape memory alloys,” Journal of Materials in Civil Engineering, vol. 19, no. 6, pp. 454–461, 2007.

[20] M. Indirli, M. G. Castellano, P. Clemente, and A. Martelli, “application of shape memory alloy devices: the rehabilitation of the S. Giorgio Church bell tower,” in Smart Structures and Materials 2001: Smart Systems for Bridges, Structures, and Highways, vol. 4330, pp. 262–273, 2001

[21] H. Tamai, Y. Kitagawa, "Pseudoelastic behavior of shape memory alloy wires and its application to seismic resistance member for building," Computational Materials Science, vol. 25, pp. 218–27, 2002.

[22] K. Wilde, P. Gardoni, and Y. Fujino, “Base isolation system with shape memory alloy device for elevated highway bridges,” Engineering structures, vol. 22, no. 3, pp. 222–229, 2000.

[23] M. Dolce and D. Cardone, “Mechanical behaviour of shape memory alloys for seismic applications 2. Austenite NiTi wires subjected to tension,” International Journal of Mechanical Sciences, vol. 43, no. 11, pp. 2657–2677, 2001.

[24] F. Casciati, L. Faravelli, and L. Petrini, “Energy dissipation in shape memory alloy devices,” Computer-Aided Civil and Infrastructure Engineering, vol. 13, no. 6, pp. 433–442, 1998.

[25] Y. Sakai, Y. Kitagawa, T. Fukuta, and M. Iiba, “Experimental study on enhancement of self-restoration of concrete beams using SMA wire,” in Smart Structures and Materials 2003: Smart Systems and Nondestructive Evaluation for Civil Infrastructures, vol. 5057, pp.

178–187, 2003.

[26] G. Song, N. Ma, and H.-N. Li, “Applications of shape memory alloys in civil structures,” Engineering structures, vol. 28, no. 9, pp. 1266–1274, 2006.

[27] A. M. Billah and M. S. Alam, “Bond behavior of smooth and sand-coated shape memory alloy (SMA) rebar in concrete,” in Structures, vol. 5, pp. 186–195, 2016.

[28] S. M. Daghash and O. E. Ozbulut, “Bond–slip behavior of superelastic shape memory alloys for near-surface-mounted strengthening applications,” Smart Materials and Structures, vol. 26, no. 3, p. 035020, 2017.

[29] C. Czaderski, B. Hahnebach, and M. Motavalli “RC beam with variable stiffness and strength,” Construction and Building Materials, vol. 20, p. 824-833, 2006.

[30] H. Tamai, Y. Kitagawa, T. Fukuta, “Application of SMA Rods to Exposed-Type Column Bases in Smart Structural Systems,” 13th World Conference on Earthquake Engineering, Vancouver, Canada, 2014.

[31] ACI Committee 224, "Control of Cracking in Concrete Structures".

[32] ACI Committee 318-14, "Building Code Requirements for Structural Concrete and Commentary".

[33] ASTM C566-13, "Standard Test Method for Total Evaporable Moisture Content of Aggregate by Drying".

[33] ASTM C39/C39M-18, "Standard Test Method for Compressive Strength of Cylindrical Concrete Specimens".

[34] ASTM C33/C33M-18, "Standard Specification for Concrete Aggregates".

[35] ASTM C78/C78M-18, "Standard Test Method for Flexural Strength of Concrete (Using Simple Beam with Third-Point Loading)".

[36] ASTM A615/A615M-18e1, "Standard Specification for Deformed and Plain Carbon-Steel Bars for Concrete Reinforcement".

[37] ASTM C143/C143M-15a, "Standard Test Method for Slump of Hydraulic-Cement Concrete".

[38] ASTM C231/C231M-17a, "Standard Specification for Deformed and Plain Carbon-Steel Bars for Concrete Reinforcement".

[39] ASTM C31/C31M-18b, "Standard Practice for Making and Curing Concrete Test Specimens in the Field".